



Historical Perspective



Bubble growth analysis during subcooled boiling experiments on-board the international space station: Benchmark image analysis

O. Oikonomidou^a, S. Evgenidis^a, C. Argyropoulos^a, X. Zabulis^{a,b}, P. Karamaoynas^{a,b}, M.Q. Raza^c, J. Sebilliau^c, F. Ronshin^{d,e}, M. Chinaud^d, A.I. Garivalis^f, M. Kostoglou^a, A. Sielaff^g, M. Schinnerl^g, P. Stephan^g, C. Colin^c, L. Tadriss^d, O. Kabov^e, P. Di Marco^f, T. Karapantsios^{a,*}

^a Department of Chemical Technology and Industrial Chemistry, Faculty of Chemistry, Aristotle University, University Box 116, 541 24 Thessaloniki, Greece

^b Institute of Computer Science, Foundation for Research and Technology, Hellas, N. Plastira 100 Vassilika Vouton, 700 13 Heraklion, Crete, Greece

^c Institut de Mécanique des Fluides de Toulouse, Université de Toulouse, UMR 5502, CNRS-INPT-UPS, 31400 Toulouse, France

^d Aix Marseille Université, CNRS, Laboratoire IUSTI, UMR 7343, 13453 Marseille, France

^e Kutateladze Institute of Thermophysics, Lavrentyev Prospekt, 1, Novosibirsk 630090, Russia

^f DESTEC, University of Pisa, Largo L. Lazzarino 1, 56122 Pisa, Italy

^g Institute for Technical Thermodynamics, Technische Universität Darmstadt, Alarich-Weiss-Str. 10, 64287 Darmstadt, Germany

ARTICLE INFO

Keywords:

Boiling
Microgravity
Bubble growth
Image processing
Edge detection
Contact angle

ABSTRACT

This work compares four different image processing algorithms for the analysis of image data obtained during the Multiscale Boiling Experiment of ESA, executed on-board the International Space Station. Two separate experimental campaigns have been performed in 2019 and 2020, aiming to investigate boiling phenomena in microgravity, with and without the presence of shear flow and electric field. A heated substrate, at the bottom of the test cell, creates a temperature profile across the liquid bulk above it. A laser beam hits a designated microcavity at the middle of the substrate, to initiate nucleation of a single, isolated bubble. In the presence of shear flow or electric field forces, the bubble slides or detaches respectively, leaving the cavity free for the nucleation and growth of a new bubble. The growth of such a bubble within the prescribed temperature profile is studied for varying experimental conditions (i.e. pressure, heat flux, subcooling temperature) by capturing high speed, black and white video images. The presence of light reflections at random locations around the bubble contour vary with bubble size and population. This, combined with the refraction induced optical distortion of vertical image dimension close to the heater, make the accurate detection of bubbles contour a real challenge. Four research teams, namely the University of Pisa (UNIP), the Institute of Fluid Mechanics of Toulouse (IMFT), the joint group of Aix Marseille University (AMU) and Kutateladze Institute of Thermophysics (IT), and the joined group of Aristotle University of Thessaloniki (AUTH), Technical University of Darmstadt (TUD) and Foundation of Research and Technology in Crete (FORTH), developed separate specialized algorithms to: a) detect bubble edges and b) use these edges to calculate basic bubble geometrical features, such as contact line diameter, bubble diameter and contact angles. These four different approaches diverge in complexity and concept. In the absence of reference measurements at microgravity conditions, measurements efficiency is evaluated based on the comparison of the estimated bubble geometrical features along with pertinent physical arguments. Results show that the efficiency of each approach varies with the nature of measurement. The studied benchmark dataset is published allowing other research groups to test further their own image processing algorithms.

1. Introduction

Boiling process is employed in different applications such as

domestic and industrial heating, food processing, cooling of electronics, power generation, vaporization, water purification etc. [1–4]. Its wide application has attracted the scientific interest for decades. However, research on boiling is an evergreen task because its complex nature

* Corresponding author.

E-mail address: karapant@chem.auth.gr (T. Karapantsios).

<https://doi.org/10.1016/j.cis.2022.102751>

Received in revised form 4 August 2022;

Available online 17 August 2022

0001-8686/© 2022 The Authors. Published by Elsevier B.V. This is an open access article under the CC BY-NC-ND license (<http://creativecommons.org/licenses/by-nc-nd/4.0/>).

benefits from further investigations with modern diagnostics at well-controlled conditions. Boiling involves the combined action of heat

the level of gravitational acceleration. In terrestrial gravity, the generation of buoyancy driven thermal liquid currents triggers natural con-

Nomenclature			
Symbol	Meaning	P_R	vertical distance of the right fitted circle's center from the shifted contact line
A	left contact point	Q	liquid flow rate
a	ellipse major axis	R_b	bubble radius
A', A''	left shifted contact point	$R_{L,c}$	radius of the left fitted circle
B	right contact point	$R_{R,c}$	radius of the right fitted circle
b	ellipse minor axis	S	bubble foot surface area
B', B''	right shifted contact point	T_{sat}	liquid saturation temperature
BC	baseline row	T_{sub}	subcooling temperature
C	curve	t_{wait}	waiting time
CAH	contact angle hysteresis	u_b	velocity of bubble gravity center
D_b	bubble diameter	UHV	electric field intensity
D_c	diameter of fitted circle	u_l	liquid velocity
D_{eq}	equivalent diameter	V	polar image
D_f	contact line diameter	V_b	bubble volume
dP	contact line vertical displacement	X	horizontal coordinate
dY	resolution on Y axis	$X_{Y,max}$	maximum horizontal coordinate of bubble contour points at 'Y' vertical coordinate
F_B	buoyancy force	$X_{Y,min}$	minimum horizontal coordinate of bubble contour points at 'Y' vertical coordinate
$F_{C,Y}$	capillary force in vertical axis	Y	vertical coordinate
F_{CP}	contact pressure force	Y_{bsln}	vertical coordinate of baseline/ contact points
$F_{I,Y}$	inertia force in vertical axis	α	left contact angle of bubbles in shear flow
$F_{T,Y}$	net force in vertical axis	β	right contact angle of bubbles in shear flow
HF	heat flux	θ, θ'	contact angles of pool and electric field boiling bubbles
I	image frame	θ_i	angular component of polar coordinate
i	azimuth	μ_j	radial component of polar coordinate
j	radial coordinate	ρ_l	liquid density
m	slope of ellipse tangent	σ_l	liquid surface tension
P	pressure	φ	ellipse rotation angle
P_L	vertical distance of the left fitted circle's center from the shifted contact line		

and mass transport, the evolution of which depends on a variety of parameters. These parameters either relate to the liquid-vapor physical properties (i.e. liquid thermal conductivity and thermal diffusivity, liquid saturation temperature and surface tension, liquid and vapor densities), to properties of the heating surface (i.e. thermal conductivity and thermal diffusivity of the material, surface area) [5–8], or to three phase properties like contact angle. The large number of key parameters affecting boiling is a drawback for the full understanding of underlying phenomena.

A significant influence on boiling is exerted by processes in the vapor-liquid-solid contact line area, as well as the dynamic contact angle of wetting inside the bubble. Currently, the heat and mass transfer processes in the area of the contact line are not completely understood because of its small size and a limited set of applied research methods [9–11]. The contact line area is often called 'microregion', especially in the context of boiling, or 'apparent contact line region'. The challenges in modeling of contact line phenomena have to do with the fact that several physical effects such as evaporation, viscous flow, surface tension, thermocapillary stresses, London-van der Waals forces, nonequilibrium effects near the vapor-liquid interface, are coupled together and are all significant in this highly localized region. This leads to difficulties in both mathematical modeling and design of experiments. The contact line is characterized by an enhanced heat transfer coefficient that was confirmed by several experiments in various configurations [12–16]. However, until now there is practically no information in the boiling literature on dynamic wetting contact angles of growing vapor bubbles.

Boiling is strongly dictated by the force of buoyancy and therefore by

vection [17]. Moreover, the high density ratio between liquid and gas phase, brings about severe distortion of bubbles shape from sphericity, being followed by the prompt detachment of boiling bubbles from the heated surface that causes intense bubbling activity. Bubbles rise creates strong back mixing of the liquid mass and introduces an extra heat convection term to the heat transfer equation. Existing relations for the estimation of heat transfer coefficient incorporate the term of gravity [18]. However, most of these empirical equations have not been tested in extra-terrestrial microgravity conditions.

In order to simplify the phenomena, boiling should be studied in the absence of gravity. The absence of gravity cancels the transfer of heat through natural convection. Another great advantage is that zero gravity hinders the detachment of bubbles and allows them to grow large at their nucleation site, thus offering the unique opportunity of satisfactory spatial detection together with significant time window for the proper examination of bubble growth during phase change. Results obtained at the absence of gravity elucidate the impact of surface tension and pressure forces on the growing volume of vapor bubbles. Relating heat fluxes with bubble dynamics facilitates in depth understanding of boiling principles. In addition, experiments at zero gravity also enable the validation of gravity term in heat transfer expressions. On another perspective, the experimental findings can be utilized for the enhancement of boiling process in space applications (i.e. thermal control of electronics, operating turbines for power generation, water purification). Up to now, most boiling works at non-terrestrial conditions refer to microgravity as part of parabolic flights, drop tower experiments etc. Some indicative examples are following. Iceri et al. 2020, investigated

the effect of microgravity on heat transfer coefficient of a flow boiling experiment, in terms of a parabolic flight campaign [19]. Wang et al. 2022 studied the effect of gravity on nucleate boiling during the release of a drop tower, aiming to enhance cooling of different sized electronic devices in different gravities [20]. Lee et al. 2022 performed temperature and image recordings of boiling incidents during a series of parabolic aircraft maneuvers, aiming to validate the corresponding CFD predictions [21]. All these attempts suffer from the important disadvantage of limited microgravity duration [22–25]. Aiming to examine boiling at prolonged microgravity conditions, a few boiling experimental campaigns were performed in the International Space Station (ISS) [26,27]. However, to obtain reliable data this kind of campaigns require the solution of several technical issues emerging during the design, construction and performance, of a well-defined, fully automated, boiling experiment.

Recently (2019–2020), a new boiling experimental campaign has been executed on-board ISS, under the umbrella of European Space Agency (ESA), as an attempt to examine the ongoing phenomena at well-controlled conditions. The experimental platform at hand, is named Multiscale Boiling Experiment. Its components and main functions are extensively described by Sielaff et al., (2022) [28]. Multiscale Boiling Experiment allows to investigate the growth of single, isolated bubbles during the subcooled boiling of a liquid, with or without the presence of shear flow and with or without the application of electric field.

The boiling test cell, illustrated at Fig. 1, consists of an aluminum block, which acquires an infrared transparent heater made by a coated barium-fluoride crystal, adjusted at its bottom plane horizontal surface. At the center of the heater there is a microcavity (the shape of the cavity is illustrated in Fig. 6 of Sielaff et al., 2022) that acts as a designated bubble nucleation site. The test cell is filled with the test fluid (FC-72, C_6F_{14}). Before each experimental run, both the test cell and the test fluid are thermalized at the desired test temperature (equal to the liquid saturation temperature, T_{sat} , minus the desired subcooling temperature, T_{sub}), using Peltier elements and a preheating/recirculating system, respectively. Moreover, the pressure (P) of the system is set at the desired level and the heater is activated at the desired heat flux (HF). After a specific waiting time (t_{wait}) elapses from the onset of the heater, a laser beam of certain duration (20 ms) is activated to overheat the cavity location and provoke nucleation of a bubble. The laser focal spot diameter is $\sim 50 \mu m$. The bubble nucleus grows in size due to liquid phase change inside the thermal boundary layer that develops above the heater. Upon bubble nucleation, each experimental run lasts for 9 s. A high-speed infrared camera is used to record the temperature field of the

heater. Moreover, a high-speed Black and White camera (BW) is used to record bubble images at 500 fps. The BW camera is placed at 5° inclination with respect to the heater. BW recordings start 1 s before bubble nucleation, so as to capture a significant number of background images (500 images), with a resolution of $20.3 \mu m/pixel$. Proper BW image processing allows to measure the temporal evolution of different geometrical characteristics of boiling bubbles, such as bubble diameter, contact line diameter and contact angles, under the effect of several experimental parameters (T_{sub} , P , HF , t_{wait}). It is important to straighten that the recorded bubble images capture the apparent contact angles of the bubble that differ from the microscopic contact angles (Young angles) at the nanoscale. Therefore, the so on called bubble contact angles are actually the apparent contact angles that slightly diverge from the real ones. Four types of experiments are conducted: 1) pool boiling, 2) boiling under shear flow, 3) boiling in the presence of an electric field and 4) boiling under the combined action of shear flow and electric field. In cases 2–4, shear flow or/and electric field are applied prior to heater activation.

Image processing is customary used as a tool to investigate the dynamics of a dispersed phase (bubbles/ droplets) in terms of multiphase systems, due to its ease of application, non-intrusive nature and high spatial resolution [29–32]. However, the existing image processing algorithms cannot be universally applied as they are quite sensitive to lighting and background image noise. In the case of Multiscale Boiling images, the development of an algorithm that is capable of identifying accurately the contour of a bubble with minimum measuring error, seems a challenging task. This is due to the presence of reflections at critical locations along the bubble contour, i.e. close to the contact points of the bubble with the heated substrate and around the bubble apex. These reflections are the result of the combined effect of lighting position and BW camera inclination towards the heater.

Fig. 2 shows some characteristic examples of light reflections close to bubble edges. On the top of all bubbles, specular highlights cause a poor contrast at the location of the bubble contour, while give rise to dominant gradient of the light at neighboring, spurious locations (Fig. 2a). Since the image background and the heated surface are both light colored, the perspective of their junction appears darker. Hence, the reflection edges on the top of a small sized bubble (i.e. right after its birth) that is growing in front of this dark region at the lower part of the image, are more intense (Fig. 2b). On the other hand, at the top of a large bubble, a poor intensity gradient appears above the dominant one (Fig. 2c, zoomed fragment of Fig. 2a). A misdetection of the upper bubble contour would introduce error at the calculation of bubble

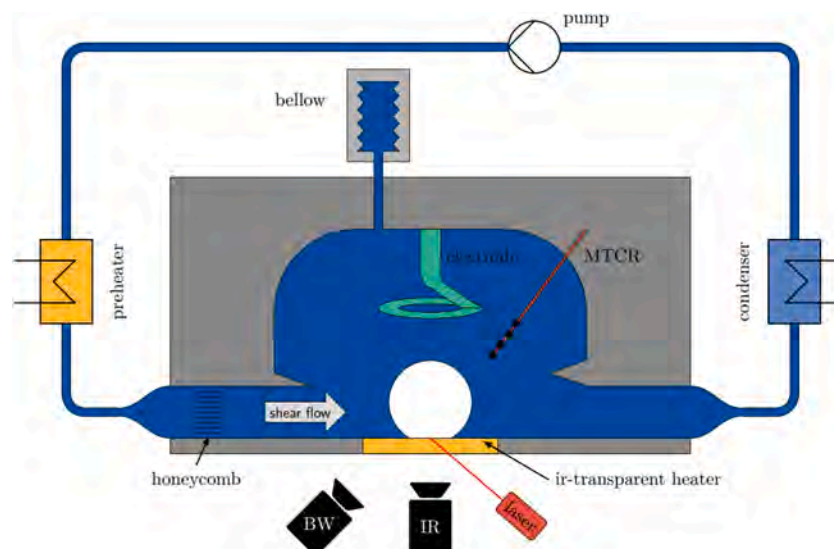


Fig. 1. Schematic description of the Multiscale Boiling experimental setup (BW: Black and White camera, IR: Infrared camera, MTCR: micro-thermocouple rack).

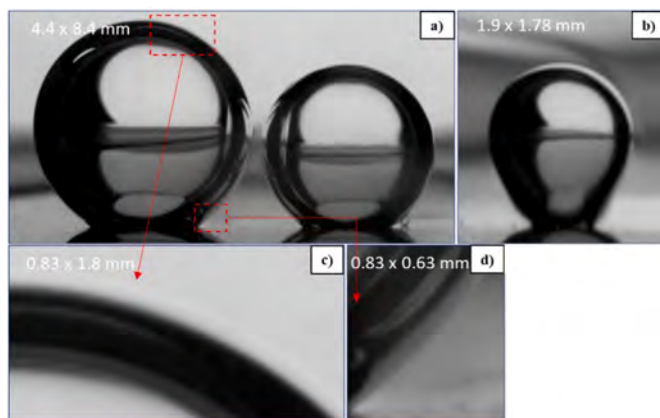


Fig. 2. Light reflections in Multiscale Boiling images at **a)** Top of the bubbles and at the region between successive bubbles in shear flow condition, **b)** Top part of new born bubbles, **c)** Top part of large bubbles, **d)** Bubble contour close to the contact points.

height. The occurrence of multiple bubbles in a single image gives rise to confounding side bubble boundaries, due to the reflections introduced by neighboring bubbles (Fig. 2a). This may cause uncertainty during bubble diameter calculations. Reflections are also present at the bubble foot region. Fig. 2d (zoomed fragment of Fig. 2a) shows how the reflections at the vicinity of the contact points induce a weak intensity gradient at the correct contour and a strong intensity gradient at neighboring spurious locations. Incorrect identification of bubble contact points would introduce error at the contact line diameter calculations, while the inaccurate definition of bubble boundaries close to the heater can result in the overestimation of contact angles.

Conventional image processing methods based on contour fitting upon a conventional background subtraction and edge detection, exhibit limitations in the situations illustrated in Fig. 2. The random character of the present reflections, varying with bubbles size and population, makes it even harder for a single algorithm to treat them.

Apart from the presence of light reflections due to the technical reasons mentioned above, additional image distortion is triggered by the propagation of heat in the liquid bulk of the test cell during each experiment [33,34]. Upon activation of the heater, heat is transferred vertically from the heated surface to the liquid layer above it, due to thermal conduction, since natural convection is not present in the absence of gravity. After t_{wait} the laser beam is activated, a bubble forms at the nucleation site and grows radially. The radial displacement of bubble boundaries pushes the surrounding liquid generating forced convection streams which deform/disturb the vertical heat conduction profile close to bubble borders. Depending on the liquid physical properties and the duration of each experiment, vertical heat flux generates a temperature gradient that is restricted only within a thin liquid layer above the heater. Thus, temperature at the majority of the liquid bulk equals the initially set experimental temperature. The intensity of this vertical temperature gradient during bubble growth increases with the applied HF, T_{sub} and t_{wait} .

After bubble nucleation, a temperature gradient develops also at the radial direction outside the bubble towards the liquid bulk. Temperature at the bubble/liquid interface equals the saturation temperature, while liquid temperature away from the bubble equals the initial experimental temperature ($T_{sat} - T_{sub}$). The intensity of this radial temperature gradient increases with the applied T_{sub} [35].

Combination of vertical and radial temperature gradients composes a 3D temperature profile in the liquid bulk [36]. Since the BW camera is tilted at 5° to the heater, light passes through successive liquid layers of different temperature before reaching the camera lenses. Refractive index of materials changes with temperature. Hence, temperature variations alter the refractive index of liquid phase and deform locally the

image of the intervening bubble. An intense temperature gradient slightly above the heater, distorts the bubble contour shape close to the contact points [37]. More specifically, the bubble perimeter near the bubble foot diverges from its original curvature and gets elongated along the vertical direction (i.e. Fig. 2b). This further impedes the accurate determination of contact angles.

Since conventional image processing algorithms fail to analyze the contour of bubbles in these special conditions, the need to develop a new special algorithm that suits the contemporary problem, arises. In this work, research groups led by four Universities, comply with the challenge of Multiscale Boiling image processing using different perspectives and develop algorithms of different complexity, accuracy and working principles. Each algorithm is presented in detail, discussing its merits and limitations. Bubble diameter, contact angles and contact line diameter resulting from these different approaches, are presented and discussed in comparison. The strategy presented in this work can be instrumental in developing future experimental setup designs, including proper background lighting arrangement, and efficient image processing algorithms for the investigation of multiphase systems. It is important to underline that this work focuses on the implementation of successful image data analysis and not on the study of bubble growth physics under the different boiling conditions.

2. Materials and methods

This part presents the algorithms developed by the research teams of (a) University of Pisa (UNIPi), (b) Aix Marseille University (AMU) together with the Kutateladze Institute of Thermophysics (IT), (c) Institute of Fluid Mechanics of Toulouse (IMFT) and (d) Aristotle University of Thessaloniki (AUTH) together with the Technical University of Darmstadt (TUD) and the Foundation of Research and Technology in Crete (FORTH), for the image processing of Multiscale Boiling experiments. All algorithms are tested in a benchmark set of representative experiments (4 pool boiling, 5 boiling under shear flow and 6 boiling under electric field). There are two phases in presenting the image processing methods. The first phase regards the detection of bubble contour, while in the second phase this contour is used to calculate bubbles' basic geometric characteristics (diameter, volume, contact line diameter, contact angles).

2.1. University of Pisa (UNIPi)

UNIPi research team developed an algorithm based on the conventional Canny edge detection technique [38]. Canny is considered among the most popular edge detection techniques, as it provides good and stable results and copes well with noise reduction. This method can be effective in well oriented experiments. In the case of bubbling experiments, backlight reflections and non-uniform backgrounds, usually result in incorrect detection of liquid-vapor interface. The choice to use a well-established and conventional algorithm is due to the necessity to deal with bubbles that are distorted by electric field. The present algorithm is the outcome of a long-term scientific experience on the design, performance and analysis of several boiling and evaporation related experimental campaigns, which aim to investigate the ongoing multiphase dynamic phenomena.

2.1.1. Phase 1: bubbles edge detection

The edge detection procedure, illustrated in Fig. 3, makes use of MATLAB "Image processing" toolbox, and can be summarized in the following steps:

1. The background image that is captured just before bubble nucleation and encaptures the fully developed thermal boundary layer above the heater, is subtracted from each end every following bubble image.

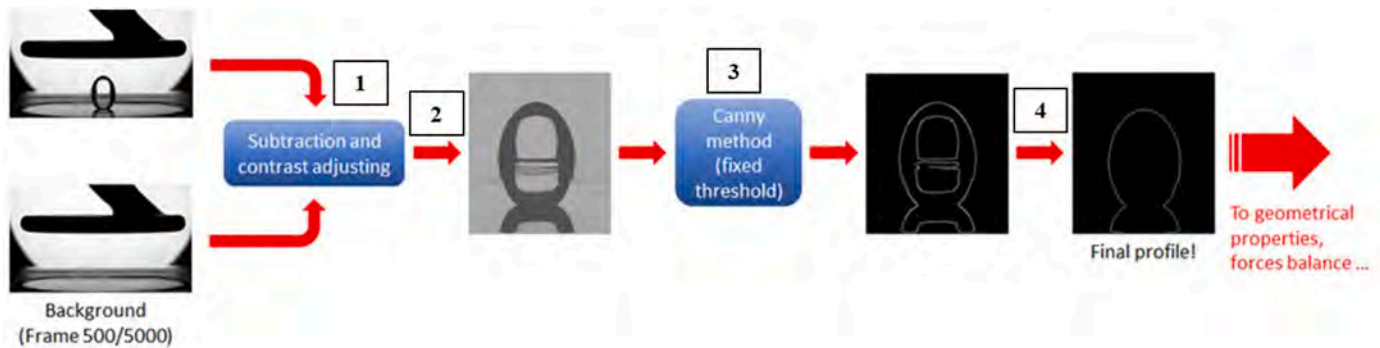


Fig. 3. The steps of UNIFI algorithm for the detection of bubble edges at the BW Multiscale Boiling images.

- The image contrast is adjusted using the *imadjust* MATLAB function. Intensity values and gamma correction factor are fine-tuned for each lighting condition, due to different average bubble size, location and population in the test cell.
- The bubble edge detection is implemented using the function:

$$\text{edge}(I, \text{'canny'}, [\text{threshold_low}, \text{threshold_high}], \text{sigma}),$$

where I is the input image (in a 2D matrix), threshold_low ($0.4 * \text{threshold_high}$) and threshold_high (0.6–0.7) parameters are set to remove the pixels of weak gradient, and sigma (set as $\text{sqrt}(2)$) is the standard deviation of the Gaussian filter (hysteresis) that tracks the weak pixels that are connected to strong pixels. Threshold parameters' values are empirically selected based on the optimum detection of bubble edges under all tested experimental conditions.

- A custom function separates the internal pixels (residual of reflections) from the boundary pixels. MATLAB functions *bwmorph* and *bwareaopen* are used several times to close the small gaps between successive edges and remove any isolated object from the image. The final bubble profile is indicated by a series of white pixels standing on a black background.

2.1.2. Phase 2: bubble geometry calculations

The bubble profile resulting from Phase 1 (see red contour in Fig. 4)

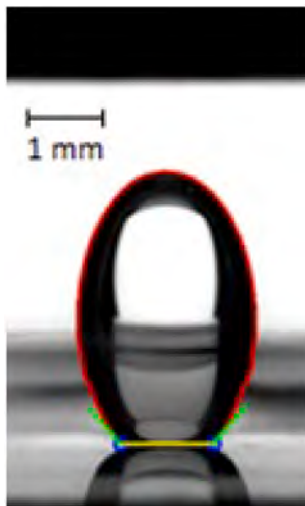


Fig. 4. Example of UNIFI algorithm output for the case of a boiling bubble under electric field. The resulting bubble contour (in red), contact line diameter (in yellow) and contact angles (in green) are superimposed on the original image. (For interpretation of the references to color in this figure legend, the reader is referred to the web version of this article.)

is processed to obtain the evolution of bubble geometry. In case of boiling under shear flow, or electric field, bubbles detach from the nucleation point and new bubbles are formed instead. To consider for the presence of multiple bubbles in a single image, bubbles isolation is performed using *regionprops* MATLAB function.

The geometry of each separate bubble derives from the calculation of its characteristic dimensions, as follows:

- Contact line diameter: The contact points are defined as the two extreme points (at the bottom left and the right side of the bubble) where the liquid-vapor interface touches the solid substrate. A custom function calculates them, as the points at which the real interface and its reflection collapse. The horizontal distance between the two contact points, gives the diameter of the contact line (see yellow line in Fig. 4).
- Bubble height: It is the maximum vertical distance between the contact point(s) and the bubble profile.
- Bubble volume and equivalent diameter: Considering the vertical axis-symmetry of bubble shape, its volume is calculated as a solid of revolution based on the Pappus–Guldin theorem. This theorem is applied to all pixels enclosed in the bubble perimeter (meaning all pixels on and inside the bubble edge). For the case of non-axisymmetric bubbles (in the presence of shear flow), an alternative method considering a stack of one pixel height circles, is applied [39]. The equivalent diameter is the diameter of a sphere with a volume equal to the calculated bubble volume.
- Contact angles: Side linear curves interpolate the pixels of the bubble contour that are subsequent to the left and the right contact points (see green lines in Fig. 4). The slope of these linear curves determines the left and the right contact angles respectively. The decision to apply a linear interpolation is considered simple and provides stable results. By fine tuning a large number of bubble images, it results that the interpolation of 3 consecutive points for bubbles smaller than 1 mm^3 and 10 consecutive points for the case of larger bubbles, is required.

Further calculations on bubble apex curvature are presented in Appendix A.

Upon completion of the calculations above, the appropriate scale factor is used to convert all length quantities from pixels to millimeters.

2.2. Aix Marseille University (AMU) & Kutateladze Institute of Thermophysics (IT)

The research team of Aix Marseille University (AMU) together with the Kutateladze Institute of Thermophysics (IT), developed their own algorithm for the analysis of Multiscale Boiling images under all different boiling cases. This algorithm is based on the combination of edge detection and bubble shape approximation techniques. In the part of edge detection, the algorithm resembles that of UNIFI. To avoid

extensive repetitions, only the differences among these two algorithms will be presented in this section.

2.2.1. Phase 1: bubbles edge detection

Fig. 5a shows the original bubble image. After the main steps of background subtraction and image binarization, this algorithm uses MATLAB functions to improve the discontinuous bubble boundaries shown in Fig. 5b. The *edge* function is applied to the original image with subtracted background to detect bubble edges using the Roberts algorithm. The result is combined to Fig. 5b. Therefore, all black pixels enclosed to the real bubble contour are converted to white ones, giving the continuous bubble contour shown in Fig. 5c. The function *strel* creates the structural element (disk with diameter 1–2 pixels), that is used in *imopen* function to reduce the noise of bubble surface detection. The *regionprops* function is used to detect all bubbles in the frame. Each of these bubbles undergoes a separate processing. The parameters of each bubble are compared with those of the same bubble at the previous frame. If a bubble does not match any of the bubbles in the previous frame, then this bubble is considered as newly formed. It is taken into account that a bubble can only form at the nucleation point. After the process of bubbles detection, each bubble is investigated individually. The baseline location (bubble foot location) is determined using the bubble reflection on the substrate. Before the final determination of bubble edges, the present algorithm extracts the pixels of bubble reflection from the images. The part of the binary image that is located below the detected bubble baseline is cropped and the bubble contour is determined using MATLAB functions (Fig. 5d).

2.2.2. Phase 2: bubble geometry calculations

Unlike the method of UNIPI, this algorithm defines bubble diameter as the maximum horizontal distance between the bubble contour side points. The contact line diameter is still considered as the horizontal distance between the left and the right contact points, while several methods are used to obtain contact angles.

Method 1: Contact angles are calculated due to the linear or polynomial interpolation of the side ending points on the bubble boundary fit, as illustrated in Fig. 6a (similarly to UNIPI method). This method can be applied to all boiling cases. In the case of pool boiling, the resulting left and right contact angles (θ , θ') are almost equal.

Method 2: Contact angles are calculated using bubble shape approximations of standard geometrical shapes. The main innovation of the present approach is the attempt to correct bubble image distortion due to light reflections. For this, the research team encounters that in the absence of external forces (encountering gravity), boiling bubbles are expected to have a spherical shape. Based on this assumption, a circular approximation is applied at the bubble boundaries for the proper description of bubble shape. To limit the error, bubble boundaries are determined considering only the regions that are free of light reflections. Since the reflection zones change with the size of the bubble, several algorithms are developed for a wide range of bubble sizes. However, in practice it is not that feasible to combine all these algorithms in one. To

solve this problem, a universal algorithm is developed considering only the bubble contour regions that are systematically free of reflections, no matter the size of the bubble. Such are the side edge regions of the bubble (contour points sideways bubble's horizontal diameter), as well as the two contact points (Fig. 6b). For the case of pool boiling, the algorithm computes the equation of the circle that passes through four trusted points, the two extrema side points of the bubble contour (X_1, Y_1 & X_2, Y_2) and the two contact points (X_3, Y_{bsln} & X_4, Y_{bsln}), using the method of least squares. Since the camera resolution is limited, the horizontal coordinates X_1 and X_2 correspond to several values of Y_1 and Y_2 , respectively. Thus Y_1 and Y_2 , are considered as the average values of these neighboring sidepoints. Contact angles of pool boiling bubbles are determined by the tangents of the fitted circle at the contact points. The spherical shape of pool boiling bubbles gives equal side contact angles ' θ '.

In the case of a high temperature gradient the part of the bubble near the heated surface is distorted in the vertical direction, so the contact angle cannot be approximated by Method 2 (Fig. 7a). However, coordinates X_1 , X_2 , X_3 , and X_4 are not influenced by this distortion. This means that neither the bubble diameter ' D_b ', nor the contact line diameter ' D_f ' are influenced by this image distortion. Therefore, the contact angle ' θ ' can be calculated using the following equation (schematically described in Fig. 7b).

$$\theta = 90 - \cos^{-1} \left(\frac{D_f}{D_b} \right) \cdot \frac{180}{\pi} \quad (1)$$

In case of shear flow imposition, in parallel to the heated surface, the attached growing bubbles are pushed left ways, resulting in slightly different left and right contact angles. This means that even though both sides of the bubble contour retain their circular perimeter, bubble shape diverges from that of a circle in the 2-D perspective. Hence, for the accurate determination of bubble contact angles under shear flow, the shape of bubbles is characterized by fitting two separate circles at the left and the right side of the bubble, based on the three trusted boundary points of each side: the two contact points and the corresponding side point at the horizontal maximum diameter of the bubble contour (Fig. 8). Left (α) and right (β) contact angles are determined by the tangents of the fitted side circles at the corresponding contact points. Shear flow images encounter a number of coexisting growing/sliding bubbles. The algorithm is capable of processing each bubble separately.

In the presence of external electric field forces, the spherical approximation is not capable to describe the elongated bubbles shape. In this case, bubbles can be fitted properly by an ellipse. Contact angles are calculated using tangents of the ellipse at the contact points (similarly to the pool boiling case, illustrated in Fig. 6b). At the presence of a high temperature gradient, the bottom part of the bubble shape is distorted. In this case, only the top half part of the bubble contour should be fitted with an ellipse. However, decreasing the number of trusted contour points, eliminates significantly the measuring accuracy.

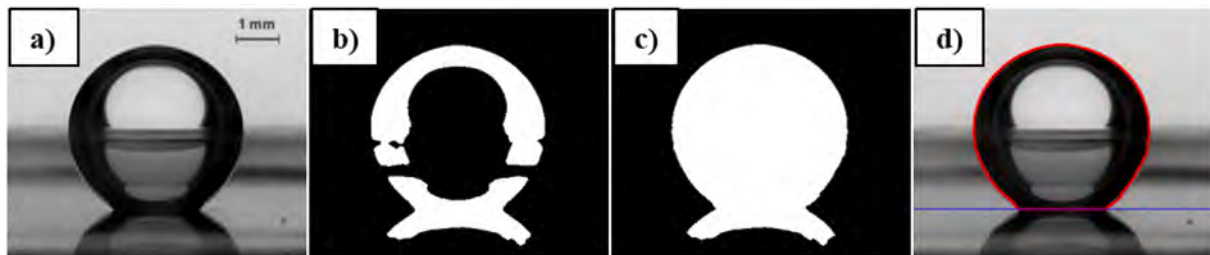


Fig. 5. The steps of AMU/IT algorithm for the detection of bubble contour in BW Multiscale Boiling images: a) Original image, b) Binarized image, c) Improved binarized image, d) Detected bubble contour in red and baseline in blue color. (For interpretation of the references to color in this figure legend, the reader is referred to the web version of this article.)

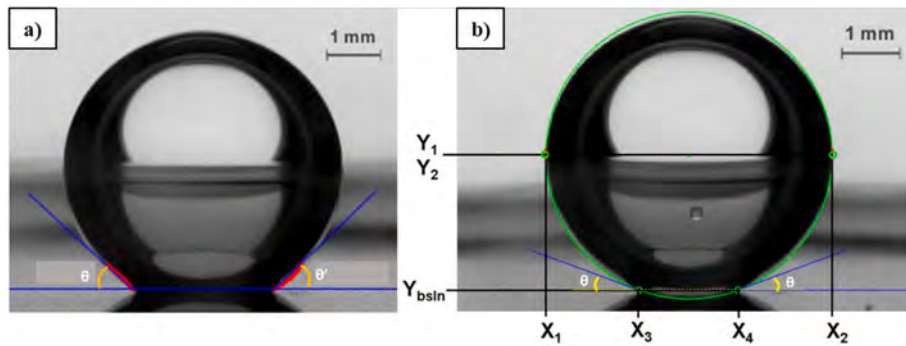


Fig. 6. Contact angles evaluation for the case of pool boiling bubbles by means of a) Bubble contour linear interpolation and b) Circular approximation methods of AMU/IT group.

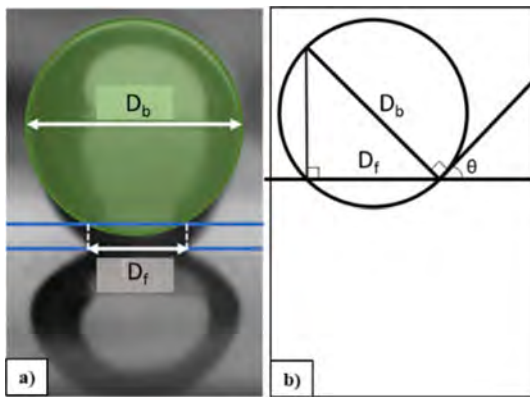


Fig. 7. a) Image distortion close to the heated surface at high temperature gradient and b) Geometrical calculation of pool boiling bubble contact angles, using the dimensions measured by the AMU/IT algorithm.

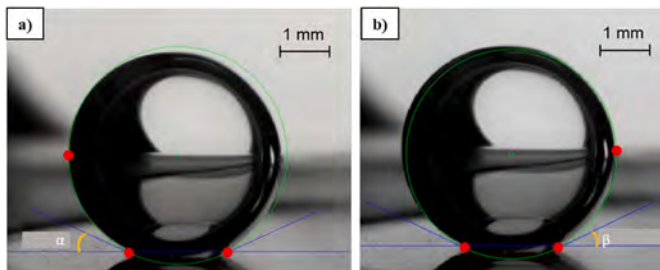


Fig. 8. a) Left contact angle and b) Right contact angle evaluation for the case of boiling under shear flow, using AMU/IT algorithm.

2.3. Institute of fluid mechanics of toulouse (IMFT)

Another research team that participates at the analysis of Multiscale Boiling Experiment BW images, comes from the Institute of Fluid Mechanics of Toulouse. This team developed an algorithm using MATLAB based Image Processing Toolbox to accomplish the detection of bubble edges.

2.3.1. Phase 1: bubbles edge detection

The present algorithm involves the main image processing steps with those presented above, however they are executed through different MATLAB commands and with another order. As illustrated in Fig. 9, at first both background and bubble images are cropped at the region of interest (Fig. 9a), to accelerate the processing procedure. All images are converted to the double precision format (im2double function), and

undergo contrast adjustment using the corresponding intensity values and image sharpening (imsharpen function) (Fig. 9b). Next, the background is subtracted from the bubble image (imsubtract function, Fig. 9c). The resulting grayscale image is binarized [im2bw(Image, Threshold) function] with a fixed threshold intensity value (Fig. 9d). Final processing regards the filling of holes (imfill function, Fig. 9e) and the removal of noise or unwanted areas (bwareopen and imopen functions, Fig. 9f).

In all tested boiling conditions, the application of a boundary fit (bwboundaries function) to the clean binary image gives the bubble contour (Fig. 10a). Often, the boundary fit misses to encounter the reflection region surrounding the top part of the bubble, since it is already excluded during the step of contrast adjustment. Therefore, the detected bubble edges slightly underfit the real bubble contour. To solve this problem, the boundary fit at the top part of the bubble is roughly adjusted by its 1–2 pixels radial movement (Fig. 10b).

2.3.2. Phase 2: bubble geometry calculations

At this phase, the research team develops an algorithm that uses the bubble contour equation to evaluate the temporal evolution of different geometrical parameters. The minimum chord length near the bubble foot (neck region) defines the position of the contact points and the contact line, since the actual contour of the bubble and its reflection collapse at the contact line location. Contact line diameter (D_f) is calculated as the distance between the contact points (Fig. 10c). Contact angles, are indicated by the slope of a 10 pixels linear fitting at the contact points region. The volume of the bubble (V_b) and its equivalent diameter (D_{eq}) are calculated based on eqs. 2 and 3, where ‘Y’ is the vertical coordinate of bubble boundary points, ‘ $X_{Y,max}$ ’ and ‘ $X_{Y,min}$ ’ are the maximum and minimum horizontal coordinates of bubble contour points at ‘Y’ vertical coordinate, and 1 pixel is the algorithm’s resolution on the Y axis (dY).

$$V_b = \frac{\pi}{4} \sum_{Y=1}^n (X_{Y,max} - X_{Y,min})^2 \times 1\text{pixel} \tag{2}$$

$$D_{eq} = \left(\frac{6 \times V_b}{\pi} \right)^{1/3} \tag{3}$$

IMFT research team follows the same approximation with AMU/IT team and treats the optical distortions by fitting bubbles contour with standard geometrical shapes, based on the prevailing boiling conditions. However, the present approach goes a step further and cancels the combined effect of both light reflection and thermal refraction on bubble images. Evaluation of the real bubble contour close to the contact points, is essential to avoid the overestimation of contact angles.

Therefore, in the case of pool boiling the bubble contour is fitted with a circle (Fig. 11a), however this time the trusted regions of the bubble contour are not selected based on the absence of light reflections, but based on the minimum refraction due to thermal inhomogeneities. Since

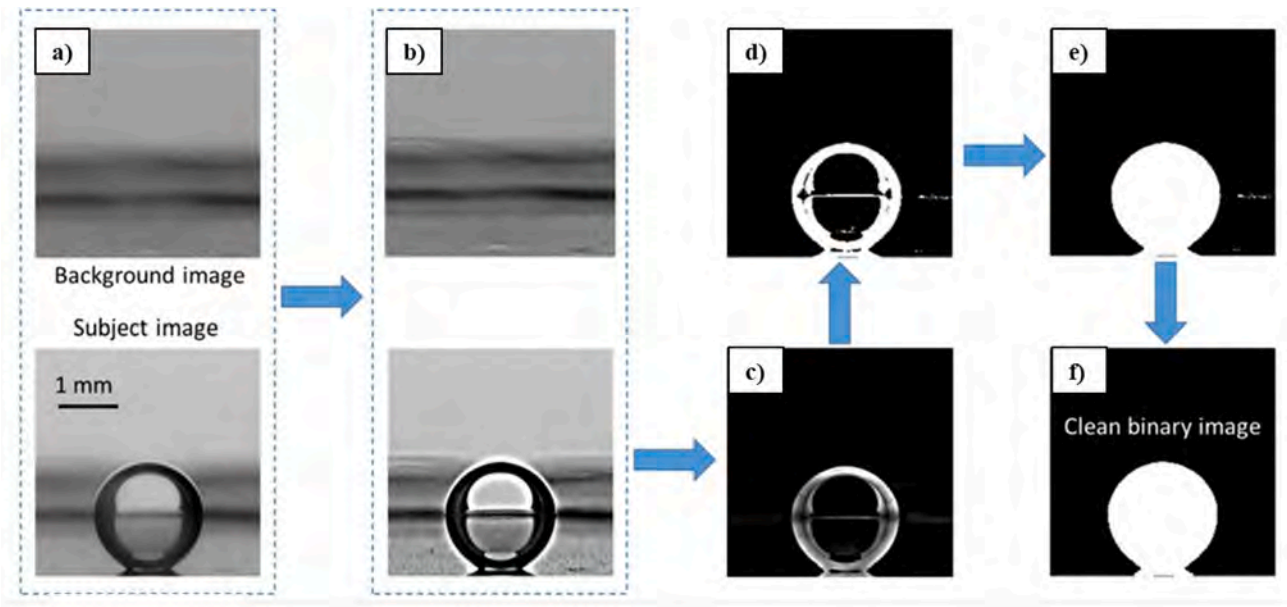


Fig. 9. The steps of IMFT algorithm for the detection of bubbles contour in BW Multiscale Boiling images: a) Image crop, b) Contrast adjustment, c) Background subtraction, d) Image binarization, e) Holes filling, f) Noise removal.

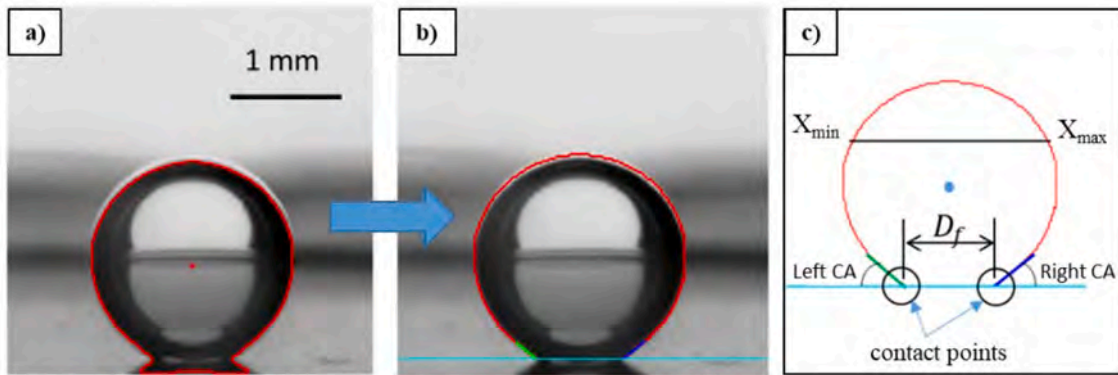


Fig. 10. The bubble contour a) As obtained by the boundary fit of IMFT algorithm, b) After compensation of light reflections on bubble apex, c) Used for the calculation of bubble geometrical features.

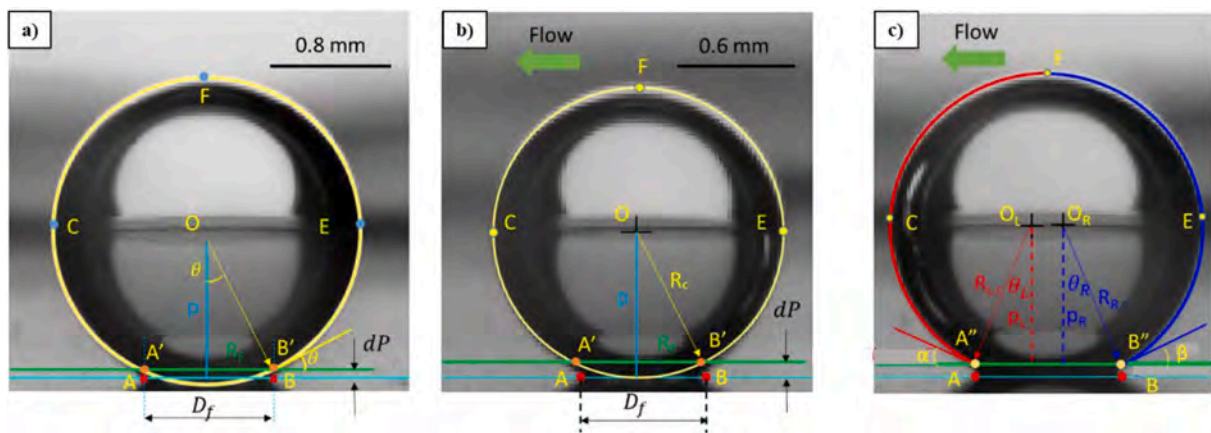


Fig. 11. Measuring of a) Contact angles of pool boiling bubbles using a circle fit approximation, b) Vertical displacement of contact points for shear flow boiling bubbles using a circle fit, c) Contact angles of shear flow boiling bubbles using side circle fits, with IMFT algorithm.

the top part of the bubble (bubble apex) is away from the vertical, thermal boundary layer that develops above the heated substrate, it can be assumed that it does not suffer refractive optical distortion. Thus, the circle fit is applied at three characteristic trusted points of the upper half part of the bubble: the two contour points on the horizontal diameter (points C and E) and the top point of the bubble apex (point F) as determined by the boundary fit.

The circle fit approach (Fig. 11a), defines the diameter of pool boiling bubbles as the diameter of the fitted circle (D_c). As expected, the contact points A and B of the distorted bubble image do not belong to the fitted circle. However, considering the absence of optical distortion along the horizontal axis, the distance of these contact points gives the realistic contact line diameter. To compensate for the refraction, contact angles are evaluated by shifting the contact points A and B in the vertical direction by dP , until they meet the fitted circle (to points A' and B'). The contact angle ' θ ' at the shifted contact points and the bubble volume ' V_b ' are calculated using eqs. 4 and 5.

$$\theta = \sin^{-1}(D_t/D_c) \quad (4)$$

$$V_b = \frac{\pi}{3}(D_c/2)^3(2 + 3\cos\theta - \cos^3\theta) \quad (5)$$

In the presence of shear flow, the shape of the bubble is not completely spherical. The effect of shear flow is to tilt the bubble towards the direction of the flow. This results in the contact angle hysteresis ($CAH = \beta - \alpha$), where ' α ' and ' β ' are the contact angles at the upstream and downstream of the bubble (Fig. 11b). Under large flow rates, CAH is considered significant. In shear flow experiments, contact angles evaluation is done in two steps. The first step, aims to calculate the contact line vertical displacement. In this step, the bubble contour is fitted by a circle that passes through points C, F & E (as in pool boiling experiments). Cord A'B' with a length equal to AB is indicated on this circle, however this time the center 'O' of the tilted bubble is not in the center of the foot diameter AB (Fig. 10b). In other words, AA' and BB' are not perpendicular to AB. The contact line vertical displacement ' dP ' is calculated by the equation $dP = p - \sqrt{(R_c)^2 - (R_f)^2}$, where ' p ' is the perpendicular distance from the center of the circle to the contact line AB, ' R_c ' is the radius of the fitted circle and ' R_f ' is the contact line radius. In the second step (Fig. 11c), the contact points are shifted vertically by distance dP towards the bubble, defining the shifted contact points A' and B' that compensate for the refraction. Circle fits are made to the left-half and right-half portion of the bubble, through the points A'CF and B'EF, respectively. The contact angles of shear flow boiling bubbles are calculated using eqs. 6 and 7.

$$\alpha = \cos^{-1}(p_L/R_{L,c}) \quad (6)$$

$$\beta = \cos^{-1}(p_R/R_{R,c}) \quad (7)$$

where, ' p_L ' and ' p_R ' are the vertical distance of the centers of the respective side fitted circles from the shifted contact line A'B'. ' $R_{L,c}$ ' and ' $R_{R,c}$ ' are the radius of the respective left and right fitted circles. Bubble volume and diameter in shear flow are calculated based on the boundary fit, using eqs. 2 and 3 respectively.

Boiling bubbles experience various kind of dynamic forces during their growth, such as capillary force, inertia, contact pressure and buoyancy. The evolution of these forces depends on the temporal evolution of bubble geometry. Moreover, in microgravity conditions the net resultant force acting on a bubble normally to the heated surface is expected to be negligible due to negligible buoyancy. Based on the facts above, IMFT evaluates its different bubble contour detection strategies (i.e. circle fit, boundary fit) by performing a force balance analysis on the bubble, normally to the heated surface. The results of this force balance analysis are presented graphically in Appendix B, while the relevant calculations are given at section S1 of the supplementary material. IMFT has applied this force balance approach in different cases as

well [40,41].

In case electric field is applied during pool boiling, bubbles are elongated in the vertical direction. In this condition, an ellipse fits the bubble contour points using the least squares method. The contact angles are determined by the tangents of the fitted ellipse at the bubble contact points (alike pool boiling case in Fig. 11a).

2.4. Aristotle University of Thessaloniki (AUTH), Technical University of Darmstadt (TUD) & Foundation of Research and Technology in Crete (FORTH)

The research team of the Aristotle University of Thessaloniki (AUTH), in collaboration with the Technical University of Darmstadt (TUD) and the Foundation of Research and Technology in Crete (FORTH), developed an algorithm that detects the bubble boundaries with higher accuracy (in the order of subpixels) and less uncertainty than that of the conventional edge detection techniques, further minimizing the error in bubble shape evolution measurements [42].

2.4.1. Phase 1: bubbles edge detection

Two independent visual feature detection methods provide the trusted points on bubble contour and the bubble foot location. These two quantities are used to compute the geometrical features of bubbles by closed-form formulae.

Selection of trusted points on bubble contour:

At first, the algorithm performs image background subtraction. The input to the computation is image frame 'I'. A coarse silhouette (blob) approximation of the bubble is obtained using Connected Component Labelling, with 8 pixel connectivity [43]. Multiple silhouettes are tracked individually. A curve 'C' is fitted to the points of each silhouette contour using least-squares. The type of curve (either a circle or an ellipse) is determined by the 2-D bubble shape in the image.

Image gradient and edge detection methods are used to detect the bubble contour trusted points. Extrema detection is set as extremely sensitive, for detecting even the faintest edges that might be part of the pursued bubble contour (Fig. 12a). To cope with the large amount of resulting edges, the acuity of the edge detector is tuned only to the edges with a compatible orientation to that of the shape of the bubble (Fig. 12b).

The region surrounding C (annulus in case of a circle, ellipse ring in case of an ellipse) is warped in a rectangular, polar image, 'V', as shown in Fig. 13a and b. In this image, columns 'i' correspond to the azimuths and rows 'j' to the radial coordinates. The image formation equation is then $V(i,j) = I((R_c + \mu_j)\cos\theta_i, (R_c + \mu_j)\sin\theta_i)$, for the circle of radius ' R_c ' and $V(i,j) = I((a + \mu_j)\cos\theta_i, (b + \mu_j)\sin\theta_i)$, for an ellipse with axes 'a' and 'b'. The angular and radial components of the polar coordinates of a point in image I, with respect to the corresponding curve C, are ' θ_i ' and ' μ_j '.

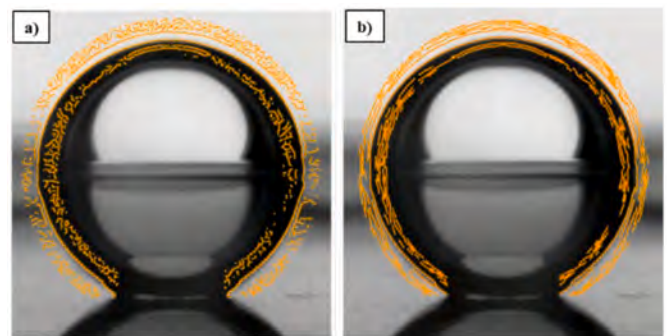


Fig. 12. Detected image edges applying a) Conventional edge detection method, b) The present proposed image polarization technique of AUTH/TUD/FORTH that gives edges with the orientation of bubble curvature.

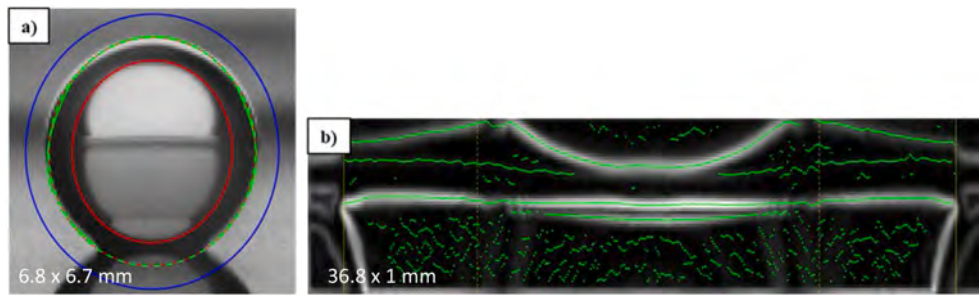


Fig. 13. a) Ring region in between blue and red ellipses surrounding curve C and b) Warped rectangular polar image V including trusted edge points, emerging from AUTH/TUD/FORTH algorithm. (For interpretation of the references to color in this figure legend, the reader is referred to the web version of this article.)

In image V, edge detection is simplified as it is performed in 1D. The vertical gradient magnitude of V is computed columnwise. The resulting image edges are the local extrema detected across the columns, with a sub-pixel accuracy. Edge detection at the vertical direction of V corresponds to that of radial direction of C. Fig. 12 compares the proposed edge detection method (Figure12b) against the widest-used generic edge detection method (Fig. 12a) [38], using a universal extremum detection sensitivity. It is observed that crucial edges near the contact points are better recovered and faint edges are more continuously recovered.

Connected edges are linked into segments, disallowing connectivity in cases of junctions (edges with more than two neighbors). As a result, all segments have two ends, each one corresponding to a particular bearing (Fig. 14a). The obtained segments are evaluated as to their compatibility to the shape of the bubble. Distinct segments that are compatible to size-dominant segments in terms of curvature are promoted for selection. Segments that are ‘covered’ by others of greater radius and angular breadth, or do not exhibit compatible curvature with the coarsely estimated bubble, are discarded (Fig. 14b). Finally, the outmost of the segment points, if any, per each polar direction is the boundary point detection for that bearing. The result is a clockwise-ordered set of points forming a contour.

Bubble foot detection:

A coarse-to-fine approach is followed to detect the baseline, using the reflection of the bubble on the substrate. The image row where the baseline occurs is initially localized at the bottom of the silhouette contour. An optimization task refines the bubble foot location (baseline), measuring the local symmetry of image regions above and below the candidate baseline row ‘BC’. The optimum baseline results from the minimum Sum of Absolute Differences cost function. The contact points, are initially approximated at the intersections of C with BC. Harris operator computes the local maximum at their neighboring regions, thus refining the estimated contact points [38]. The final baseline row, is the average of the Y-coordinates of the contact points.

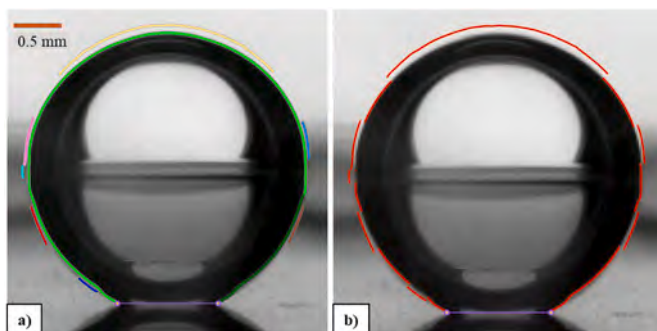


Fig. 14. a) Distinct segments resulting from the connection of shorter image edges, b) Final selection of trusted points on bubble contour after discarding the overlapped parts of continuous segments, using the algorithm of AUTH/TUD/FORTH.

2.4.2. Phase 2: bubble geometry calculations

Contact line diameter is calculated as the horizontal distance of the two contact points. To calculate the rest of the bubble geometric characteristics, the selected trusted points of the bubble contour are fitted with standard geometrical shapes, as indicated by the boiling conditions and the 2-D bubble shape in the image.

In pool boiling experiments, circle fit is applied. In general, the region of interest for the trusted points selection can be adopted as desired based on the needs. By fine tuning the trusted points selection pattern, it turns out that selecting trusted points at the:

- Two side extrema contour regions and the contact points regions (‘four points fit’ technique), the fitted circle diverges from bubble shape for the case of small bubbles.
- Top part of the bubble (regions of interest is at 9–3 o’clock, ‘top hat’ technique), the bottom part of the bubble is not that well oriented by the fitted circle.
- Top part of the bubble, using extra trusted points at the bottom part of the bubble (‘full hat’ technique), helps for the better determination of the bubble contour (especially during early life of the bubble).

Even if the full hat approach is considered the most appropriate to describe the bubble shape, the top hat approach is preferred, to compensate for refractive optical distortion. Bubble diameter is considered that of the fitted circle. The bubble volume is calculated using eq. 5 for spherical caps.

Geometry calculations using the fitted circle in combination with the detected bubble foot, can give the contact angles. Since contact points (red circles A, B) are not points of the circle, they are vertically displaced till they meet the circle perimeter at points A’, B’ (yellow circles, Fig. 15). Circle tangents at the displaced contact points determine the contact angles using eq. 4.

Circle fit is applied to measure the diameter of boiling bubbles in shear flow as well. Trusted points are selected at the top part of the bubble (top hat approximation, 9–3 o’clock). Flow is expected to cause diverging left and right contact angles. To account for their estimation, left and right side circle fits are applied separately at the corresponding

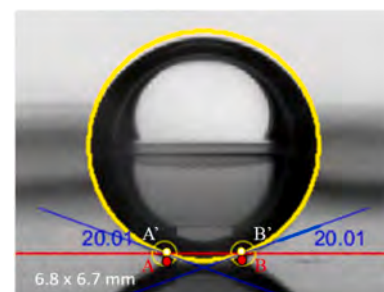


Fig. 15. Contact angles measurement, applying a circle fit on the trusted points of pool boiling bubbles, as detected by AUTH/TUD/FORTH algorithm.

top-left (9–12 o'clock) and top-right (12–3 o'clock) trusted points (Fig. 16a and b). Since the bubble contour is not axi-symmetric, the displaced contact points A' and B' are non collinear. Contact angles are calculated separately at the corresponding contact points, using eqs. 6 and 7.

The trusted points (full hat approach) of electric field bubbles are fitted with a rotating ellipse of a center (x, y), a major axis 'a', a minor axis 'b' and a rotation angle along the x axis 'φ'. In the absence of shear flow, φ is expected to be close to zero and side contact angles are expected to be equal. Fig. 17 shows the calculation of contact angles using the ellipse tangents at the projected contact points of A and B. The equation of the tangent line to an ellipse $\frac{X^2}{a^2} + \frac{Y^2}{b^2} = 1$ at the contact point (X_A, Y_{bsln}) is $\frac{X \cdot X_A}{a^2} + \frac{Y \cdot Y_{bsln}}{b^2} = 1 \Rightarrow Y = \frac{-X_A \cdot b^2}{Y_{bsln} \cdot a^2} \cdot X + \frac{b^2}{Y_{bsln}}$ with a slope, $m = \frac{-X_A \cdot b^2}{Y_{bsln} \cdot a^2}$. Thus, contact angle is $\theta = \text{atan}(m)$.

2.4.2.1. Measurement uncertainty. The measurement error of all algorithms for the identification of certain 2-D points in Multiscale Boiling images is $\pm 20 \mu\text{m}$. This number derives from combining the algorithm's detection resolution (± 1 pixel) with the resolution of bubble images ($20 \mu\text{m}/\text{pix}$). The measurement error refers to the identification of the contact points and thus the baseline location, the measurement of bubble diameter, contact line diameter and other bubble geometric features. Bubble diameter measurement depends on the horizontal location of the two extreme side points of the bubble contour. This corresponds to $\pm 20 \mu\text{m}$ average measurement error, implying that the minimum bubble diameter that can be measured with a reasonable error is about 0.2 mm. Contact points determination includes $\pm 20 \mu\text{m}$ error for both X and Y axis. Contact line diameter is roughly half of the bubble diameter, so the measurement error has a significant contribution to its calculation. Contact angles measurement depends both on the correct determination of contact points and bubble contour.

As an indication, for a small bubble of 1 mm diameter, error of bubble diameter calculation is less than $\pm 2\%$ and error of contact line diameter calculation is less than $\pm 4\%$. For a large bubble of 14 mm diameter, error of bubble diameter calculation is less than $\pm 0.15\%$ and error of contact line diameter calculation is less than $\pm 0.3\%$. For bubbles of small size (< 1 mm), the wrong detection of baseline location may cause significant error to the calculation of contact angles. To minimize this error, the baseline location is considered as the average value of several (consecutive) processed bubble frames.

Contact angles measurement is a derivative quantity. Error in measuring bubble contact angles results from error in the detection of bubble contact points and bubble contour close to the contact points. Incorrect detection of bubble contour near the contact point due to the presence of light reflections (as shown in Fig. 2d) is one of the major error aspect when contact angles are measured with linear approximation of the boundary fit (on 10 pixels close to contact points). This error is estimated as $\sim 12^\circ$ with the root mean square deviation of different

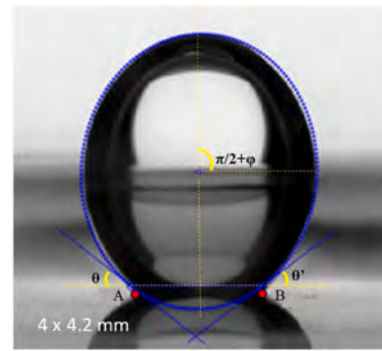


Fig. 17. Contact angles measurement of electric field boiling bubbles using the rotating ellipse fit of AUTH/TUD/FORTH method.

contact angles during bubble lifetime. The contact angles measurement is also sensitive to the number of bubble contour pixels that are linearly interpolated. The difference between interpolating 5 pixels or of 10 pixels, is about 5° . For the boundary fit cases, the maximum contact angle measuring error resulting from the cumulative effect of light reflections and number of linearly interpolated pixels is estimated to be $\sim 13^\circ$.

The uncertainty in measuring bubble contact angles using a circle fit approximation is sensitive to the exact location of trusted points on the bubble contour and the bubble foot diameter. The location of these points varies by ± 1 pixel and the corresponding uncertainty in contact angle measurement using circle fit for pool boiling bubbles is $< 2^\circ$. This error is calculated using eq. 4. The corresponding error for the case of boiling bubbles under shear flow is estimated $\sim 6^\circ$. This larger error value is attributed to the fact that shear flow bubbles are smaller in size relatively to the pool boiling bubbles. Finally, the uncertainty in measuring the contact angles of electric field bubbles using ellipse fit is calculated $\sim 3^\circ$.

3. Results

This section presents the raw measurements of the basic geometrical bubble features, resulting from the image analysis of some indicative pool, shear flow and electric field benchmark runs of the Multiscale Boiling Experiment. These features are the contact line diameter, the bubble characteristic dimensions (i.e. diameter, height) and the contact angles. Bubble volume measurements are not presented in this part, since bubble volume evolution follows the same trend as bubble diameter. Image processing is performed using the specialized algorithms of different complexity and concept, developed by UNIPI, AMU/IT, IMFT and AUTH/TUD/FORTH research groups.

3.1. Pool boiling experiments

Figs. 18 – 20 present the contact line diameter, the diameter and the contact angles of two pool boiling bubbles, growing under the same HF and different P, T_{sub} , and t_{wait} conditions. In experiment (a), bubble growth is investigated for 5.5 s, as by that time the bubble reaches the electrode at the upper part of the boiling test cell and its spherical shape starts deforming. Experiment (b) stops at 5 s, since then, a new bubble generates close to the bubble foot, disturbing the flow field around the primary bubble and resulting in intense oscillation of its boundary shape.

The calculation of contact line diameter is simple as it only requires to detect properly the horizontal location of the two bubble contact points in the image. Fig. 18a and b show the evolution of contact line diameter for the two experiments, as calculated by the four different algorithms. As expected, the resulting curves do not experience significant differences and their overall variation is $< 5\%$. In case of Fig. 18a, 3

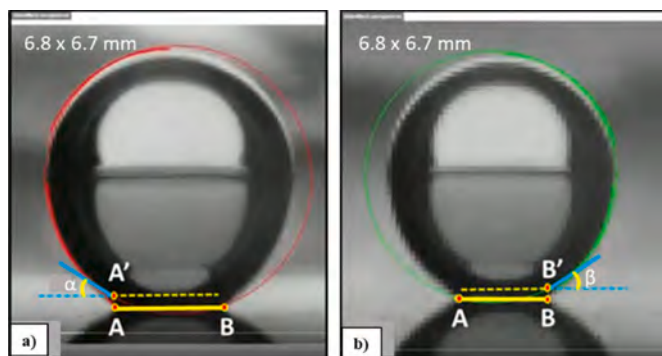


Fig. 16. Contact angles calculation using the a) Left and the b) Right circle fit of shear flow boiling bubbles, with AUTH/TUD/FORTH method.

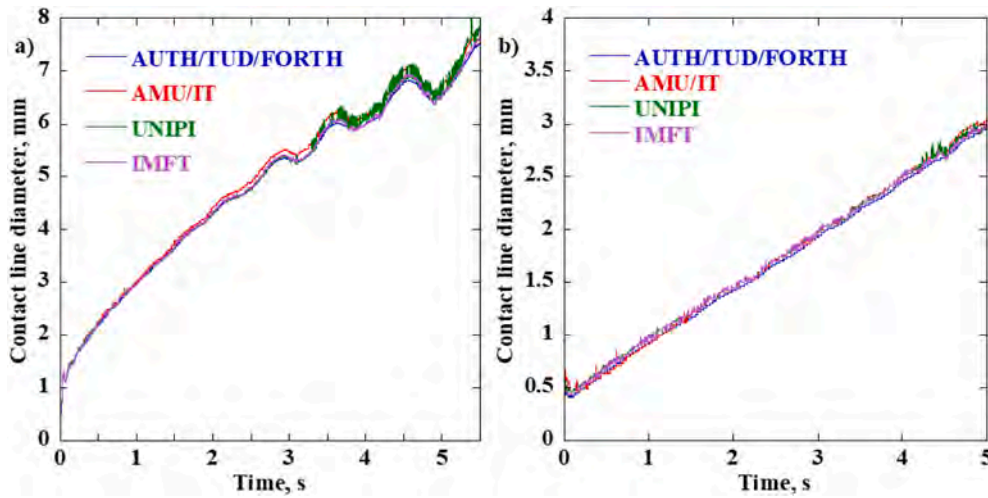


Fig. 18. Contact line diameter as a function of time for pool boiling experiments: a) $P = 500$ mbar, $T_{sub} = 1$ K, $HF = 1$ W/cm², $t_{wait} = 5$ s, b) $P = 750$ mbar, $T_{sub} = 3$ °K, $HF = 1$ W/cm², $t_{wait} = 2$ s.

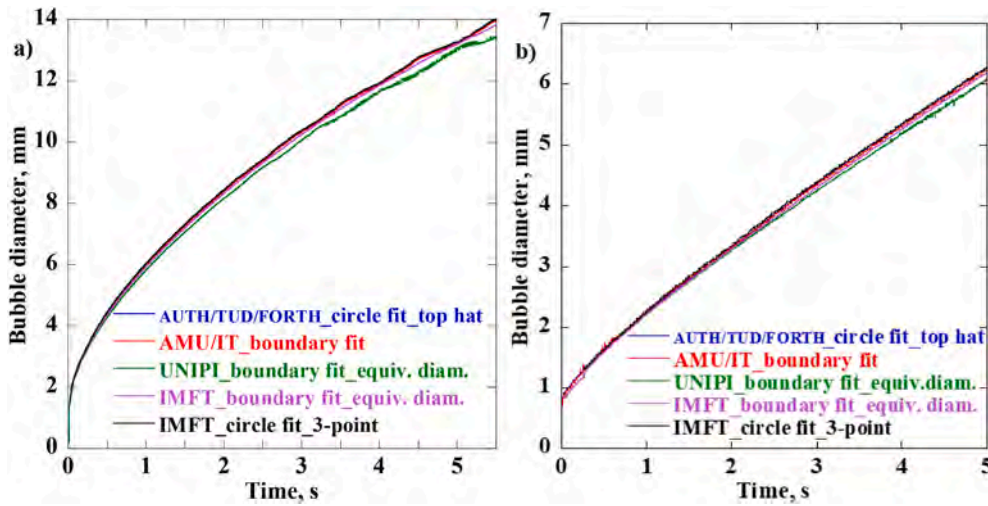


Fig. 19. Bubble diameter as a function of time for pool boiling experiments: a) $P = 500$ mbar, $T_{sub} = 1$ K, $HF = 1$ W/cm², $t_{wait} = 5$ s, b) $P = 750$ mbar, $T_{sub} = 3$ °K, $HF = 1$ W/cm², $t_{wait} = 2$ s.

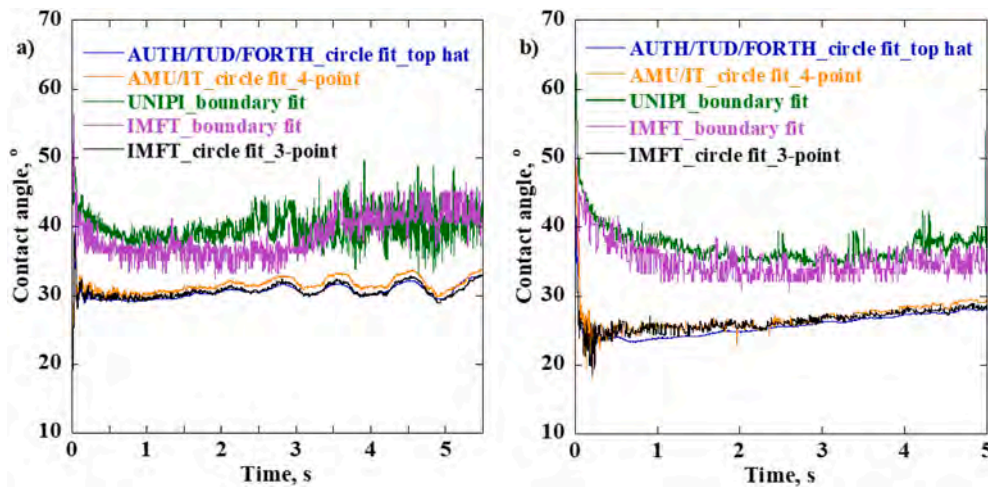


Fig. 20. Contact angle as a function of time for pool boiling experiments: a) $P = 500$ mbar, $T_{sub} = 1$ K, $HF = 1$ W/cm², $t_{wait} = 5$ s, b) $P = 750$ mbar, $T_{sub} = 3$ °K, $HF = 1$ W/cm², $t_{wait} = 2$ s.

s after nucleation the bubble foot starts oscillating radially to the nucleation point, resulting in fluctuating values of contact line diameter. At this oscillating part, UNIPI measurement gives some noise compared to the other methods. This can be explained by the fact that UNIPI edge detection process does not consider the presence of light reflections in the images. Thus, the rapid and continuous back and forth displacement of contact points during bubble oscillation, creates some noise in the resulting contact line diameter. In the case of Fig. 18b, the contact line diameter follows linear increase in time.

UNIPI and IMFT research teams use the bubble boundary fit to calculate the bubble volume and express the bubble diameter through the derived equivalent diameter. Since the spherical shape of bubbles attached on a surface is never complete, the equivalent diameter is expected to be smaller than the real bubble diameter. AMU/IT team calculates the bubble diameter as the maximum horizontal distance of the bubble boundary fit points. As a second attempt, IMFT fits the bubble with a circle (at the 2 extreme side points and the highest point of the bubble contour) and uses the diameter of this circle to determine the bubble diameter. On the same manner, AUTH/TUD/FORTH measures the diameter of the bubble with a circle that is fitted at the trusted points on bubble's top half part (top hat circle fit). Fig. 19 shows that all methods result in quite similar bubble diameter measurements, as in both experiments (a) and (b) their overall variation is <5%. However, UNIPI's boundary fit method results in slightly smaller bubble diameters, mostly at the second half of the bubbles' lifetime. The corresponding IMFT equivalent diameter values prove that the smaller UNIPI bubble diameters are not due to the indirect nature of the measurement. This discrepancy is mostly attributed to the inability of the method to encounter light reflections during edge detection.

The bubbles grow radially to the nucleation point and stay attached to the heater, during pool boiling in microgravity. Thus, contact angles are not expected to change much during bubble growth, while left and right contact angles are equal. In Fig. 20, UNIPI and IMFT research teams measure the contact angles by the linear interpolation of the bubble boundary fit points close to the contact points. AMU/IT, IMFT and AUTH/TUD/FORTH teams fit pool boiling bubbles with a circle at 4 points (2 extreme side points and 2 contact points), 3 points (2 extreme side points and highest point of bubble) and all trusted points on bubbles top half part, in respect. Using the tangents of these fitted circles at the bubble contact points, they determine contact angles. It is a common observation in both experiments (a) and (b) that boundary fit and circle fit methods, give quite different contact angle measurements. As underlined in the previous section, the proper measurement of contact angles depends on the accurate detection of the contact points location and the bubble curvature at the contact point regions. Even though the UNIPI method does not encounter light reflections in this detection, it gives only slightly higher contact angle values to those resulting from the IMFT boundary fit method that corrects the bubble contour by including its surrounding light reflections. The moving angular location of the light reflections around the bubble, creates intense noise when contact angles are calculated based on the boundary fit. At the oscillating part of the bubble growing in experiment (a), the noise of the UNIPI measurement is more intense. On the other hand, all three circle fit methods encounter the light reflections around the bubble contour, but also compensate for the refraction close to bubbles foot. Correcting the refractive image distortion, makes the circle fit methods result in lower contact angle values that coincide to each other. The contact angles measured using the circle fit allow to satisfy intrinsically the force balance on the bubble all along its growth, whereas the contact angles measured from the bubble boundary fit lead to an overestimation of the capillary force as pointed out in Appendix B. Furthermore, fitting the contour of a bubble with a circle, stabilizes and rounds the bubble contour at the contact points region. Therefore circle fit acts like a smoothing process and limits the noise of contact angle measurements. The subpixel accuracy of AUTH method, seems to eliminate further the measuring noise. Concluding, for experiment (a) UNIPI and IMFT

boundary fit methods give 10–30% higher contact angles than circle fit approximations. The corresponding percentage for experiment (b) is 30–70%.

Contrary to the subcooled related bubble oscillations during boiling in normal gravity, no oscillation incidents are detected in the present experimental cases. This can be either due to the low subcooling levels (<5 K) or due to the absence of buoyancy force that counteracts condensation and results in bubble oscillations.

3.2. Shear flow boiling experiments

Under the presence of shear flow, bubbles detach from the nucleation point when they are still small in size and free the cavity for the generation of a new bubble. Fig. 21 shows the evolution of contact line diameter and bubble diameter during an indicative benchmark, shear flow Multiscale Boiling experiment, as measured by the four different research teams. Contact line diameter and bubble diameter are calculated as in pool boiling. In shear flow IMFT-circle fit bubble diameter is not applied. Fig. 21a and b present data only for 1 s, as they show the growth of the 1st bubble until it detaches from the nucleation point and slides towards the cell's exit. Here, bubbles can be even one order of magnitude smaller than those found in pool boiling and, thus, differences in algorithm concepts can cause non-negligible variation of measured quantities. Specifically, UNIPI method, which does not encounter the presence of light reflections, results in pretty higher contact line diameter and slightly higher bubble diameter. Also, AMU/IT method gives 20% higher contact line diameter values, since it does not focus on correcting light reflections at the contact points. Inertia induced oscillations during the first milliseconds of bubble growth, cause this strange trend at the evolution of contact line diameter and bubble diameter. Moreover, oscillations are detected during the evolution of bubble diameter. Even though in this experiment the subcooling temperature is not that high (3 K), oscillations are introduced probably because liquid flow limits the thermal boundary layer, thus exposing great part of the bubble surface to the subcooled liquid bulk. Fig. 21 is a strong indication that all algorithms are able to follow bubble oscillations of high frequency. Again, the subpixel accuracy of AUTH method limits the noise in both measurements.

Fig. 22 shows the contact angle measurements for the same shear flow experiment. Here, left and right contact angles are not equal and they are presented separately. UNIPI and IMFT measure left and right contact angles with a linear interpolation of the bubble boundary fit close to the contact points. AMU/IT applies side circle fit at 3 points (1 side extrema point and 2 contact points), IMFT as a second approach applies circle fit at 3 points (highest point, side extrema point and projected side contact point) and AUTH/TUD/FORTH applies side circle fit at the side, top half of the bubble. As in the case of pool boiling bubbles, boundary fit methods give higher contact angle measurements than side circle fit approaches. Specifically, IMFT left contact angle is 100–150% higher and UNIPI 170% higher, while both IMFT and UNIPI right contact angles are ~100% higher. Also, the side circle fit of AMU/IT results in 25–50% higher values than the other two circle fit methods. The reason is the same as in pool boiling runs. All of these three methods miss to correct the refraction induced optical distortions, while UNIPI method does not either consider the light reflections. In terms of noise, measuring contact angles on the boundary fit gives more noise than using a circle fit attempt for the calculations. The intense noise detected at the IMFT side circle fit measurements is because the non-vertical projection of the contact points (see 2.3.2 section) changes the location of the fitted circle. The results can be improved by a temporal filtering.

Fig. 23a presents the evolution of left and right contact angles during the growth of a bubble in a shear flow experiment, as measured by the AUTH/TUD/FORTH method. These measurements prove that, as expected, when a bubble grows in a left wise liquid flow, the left contact angle is smaller than the right contact angle. During the first

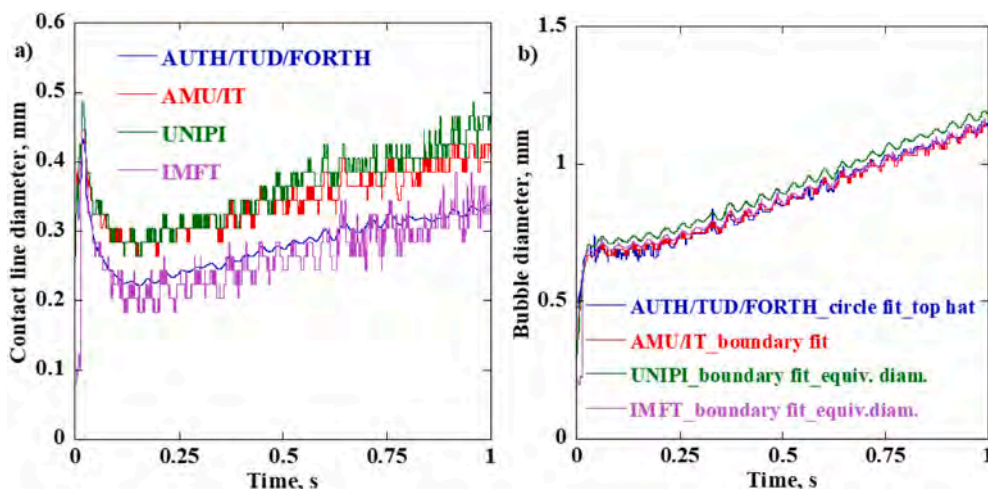


Fig. 21. a) Contact line diameter and b) Bubble diameter as a function of time for a shear flow experiment: $P = 1000$ mbar, $T_{sub} = 3$ K, $HF = 0.5$ W/cm², $Q = 500$ ml/min, $t_{wait} = 2$ s.

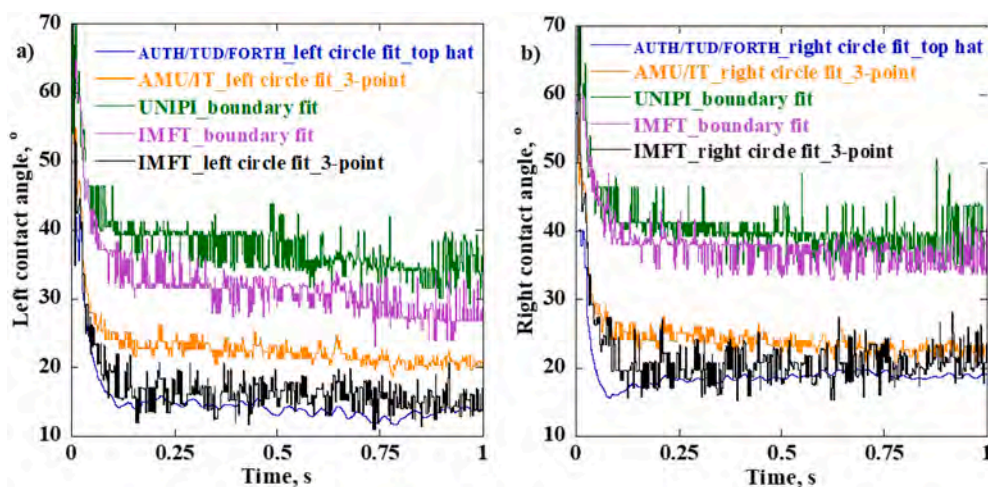


Fig. 22. a) Left contact angle and b) Right contact angle, as a function of time for a shear flow experiment: $P = 1000$ mbar, $T_{sub} = 3$ K, $HF = 0.5$ W/cm², $Q = 500$ ml/min, $t_{wait} = 2$ s.

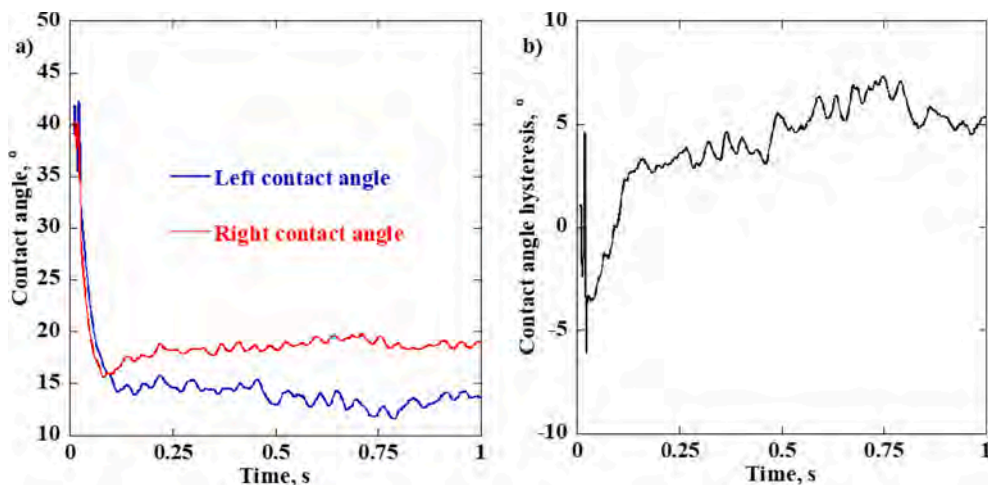


Fig. 23. a) Comparison of left and right contact angles evolution as computed by AUTH/TUD/FORTH algorithm employing side circle fitting and b) The resulting contact angle hysteresis for a shear flow experiment under $P = 1000$ mbar, $T_{sub} = 3$ K, $HF = 0.5$ W/cm², $Q = 500$ ml/min, $t_{wait} = 2$ s.

milliseconds of bubble growth, there is an abrupt, inertia induced, bubble shape change, that gives this rapid decrease of both contact angles. It is interesting to note that the corresponding CAH (Fig. 23b) is roughly similar for AUTH/TUD/FORTH, IMFT boundary fit and IMFT circle fit, despite different values of the left and right contact angles for different methods.

3.3. Electric field boiling experiments

The imposition of an electric field during boiling, results in the formation and growth of axisymmetric, elongated bubbles. In this case, the shape of a bubble is described by giving its dimensions in both x and y axis. For this purpose, UNUPI and IMFT use the boundary fit of these bubbles to calculate the equivalent diameter and the bubble height. It is important though to underline that since electric field bubbles are not spherical, the determination of bubble's horizontal dimension using the equivalent diameter introduces significant error. Fig. 24 shows the dimensions of the 1st bubble that grows in an indicative electric field benchmark Multiscale Boiling experiment, as results from the two different boundary fittings. Bubble growth is presented from nucleation until just before the bubble detaches from the heater. As UNUPI edge detection does not detect light reflections, it results in slightly lower bubble height values than IMFT boundary fit method. For the same reason, UNUPI method is expected to result in slightly lower equivalent diameters than IMFT method, however calculations show the opposite behavior. This can be explained with some differences in the boundary detection methods, that include or exclude pixels also from the bubble sides, thus influencing volume and equivalent diameter evaluation.

AMU/IT, IMFT and AUTH/TUD/FORTH teams describe the growth of electric field bubbles by fitting an ellipse at the detected bubble boundaries. The difference is that AMU/IT and IMFT apply static ellipses, centralized to the Cartesian system, while AUTH/TUD/FORTH applies a rotating ellipse. Except for the determination of the minor and the major axis, the rotating ellipse needs the definition of the degree of rotation, to be fully described. Fig. 25 shows the minor and major axis evolution of ellipses applied by the three teams to fit the growth of the 1st bubble, at the same electric field experiment presented in Fig. 24. Fig. 25 shows that the ellipse fittings of all teams coincide, as the rotating angle of AUTH/TUD/FORTH ellipse is around 1° for the entire bubble growth. As expected, the major axis of the fitted ellipse is larger than the corresponding vertical dimension of the bubble boundary fit (bubble height, Fig. 24a) where the bottom part of the elliptical bubble is truncated by the surface of the heater. Respectively, the resulting minor axis of the fitted ellipse is smaller than the corresponding horizontal

dimension of the bubble boundary fit (equivalent diameter, Fig. 24b).

The left and right contact angle measurements of this growing electric field bubble, are presented in Fig. 26. These measurements result from the boundary and ellipse fittings discussed above. Fig. 26 also includes the contact angle measurements of AMU/IT boundary fit. Comparing Fig. 26a and b, it seems that left and right contact angles are very close. This is expected since there is no flow to tilt the bubble. Moreover, this is verified by the 1° rotation of AUTH ellipse fit. It is important to underline that ellipse fit is used as an attempt to obtain a smooth and robust measurement of the bubble geometry (dimensions and contact angles). Thus, for electric field bubbles, contact angle measurements resulting from boundary fittings are expected to be equal and more noisy than those resulting from the ellipse fittings. Ellipse fit and boundary fit measurements should coincide as they both encounter the bottom part of the bubble contour (close to the contact points) without treating somehow the refractive image distortion. In practice, this happens for the case of UNUPI method, but not for the cases of AMU/IT and IMFT boundary fits. A possible explanation here is that the presence of light reflections close to the bubble contact points introduces error at the selection of trusted bubble contour points with IMFT and AMU/IT boundary fit methods. Thus, linear interpolation of these trusted points result in larger contact angle values.

The measurement of contact line diameter is not presented in the case of electric field bubbles as it resembles the strategy followed for pool and shear flow bubbles.

4. Discussion

The following highlights emerged from extensive application of the algorithms to experimental data: Regarding edge detection, a) UNUPI method does not consider the light reflections around the bubble for bubble contour evaluation, b) AMU/IT method encounters bubble regions that are systematically free from light reflections, c) IMFT's algorithm performs a rough correction at the top part of the bubble by including the light reflections at the bubble contour, and d) AUTH/TUD/FORTH algorithm is sensitive enough to treat the light reflections around the hole bubble periphery with a subpixel accuracy, resulting in a series of trusted points surrounding the bubble image. UNUPI and IMFT teams use the resulting boundary fittings to calculate the desired bubble geometric features. As an alternative approach, AMU/IT, IMFT, and AUTH/TUD/FORTH teams fit the detected bubble contour with standard geometrical shapes (circle or ellipse), in order to a) provide smoother bubble shape measurements and/or b) manage to correct the vertical bubble image distortion resulting from the thermal gradient

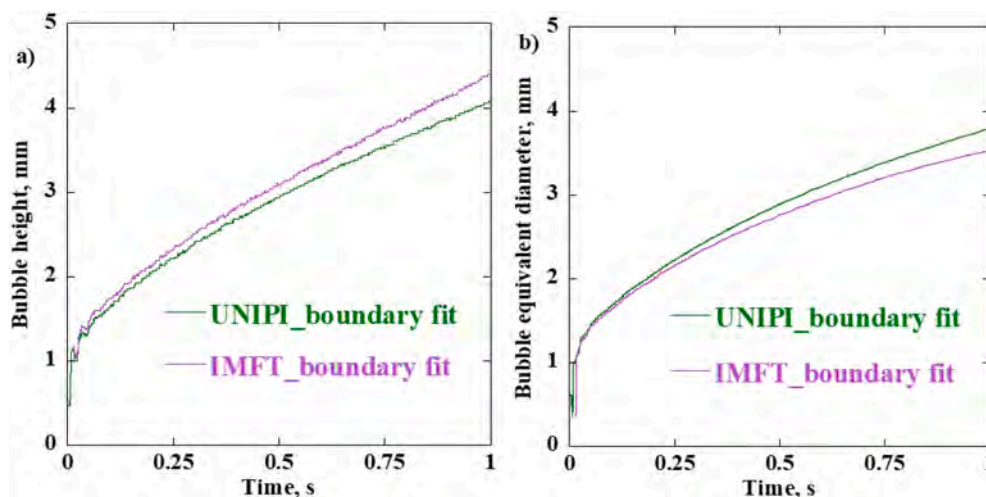


Fig. 24. a) Bubble height and b) Bubble equivalent diameter as a function of time for an electric field experiment: $P = 600$ mbar, $T_{\text{sub}} = 5$ K, $HF = 1.0$ W/cm², UHV = 15 kV, $t_{\text{wait}} = 10$ s.

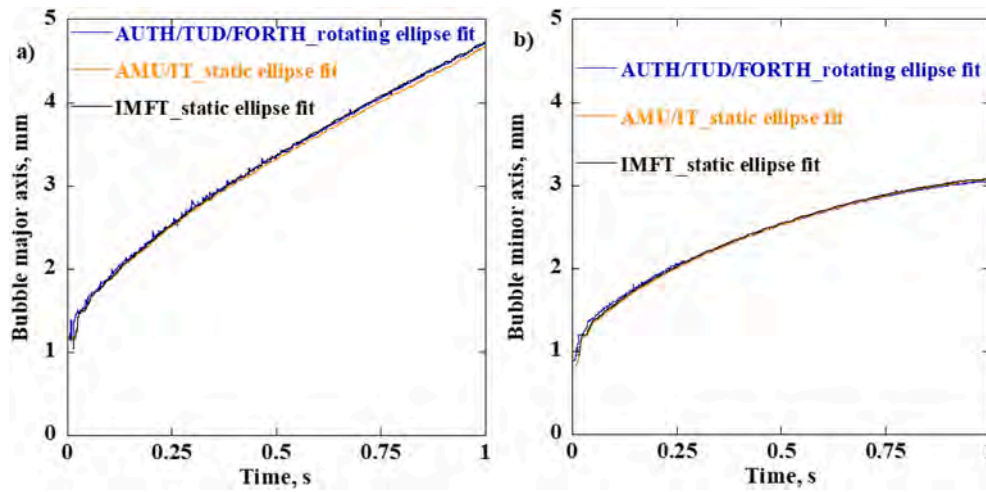


Fig. 25. a) Bubble major axis and b) Bubble minor axis as a function of time for an electric field experiment: $P = 600$ mbar, $T_{\text{sub}} = 5$ °K, $HF = 1.0$ W/cm², $UHV = 15$ kV, $t_{\text{wait}} = 10$ s.

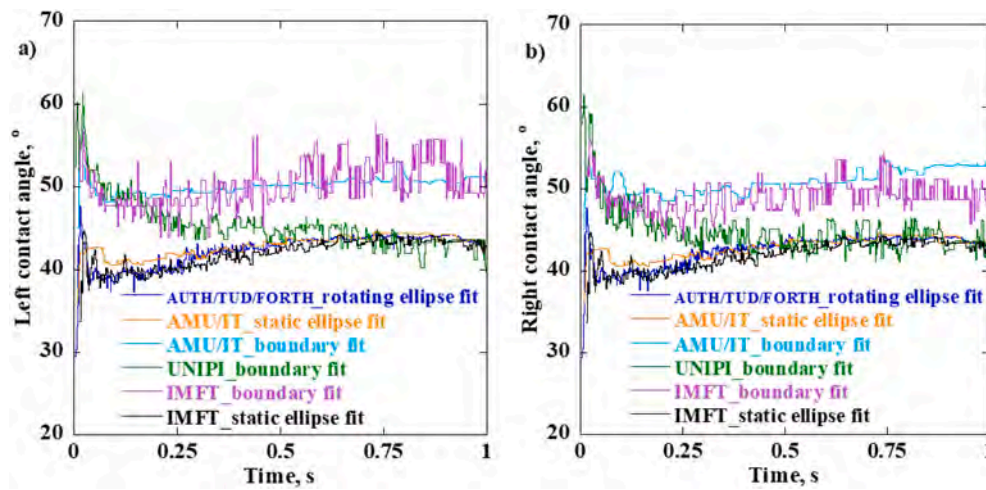


Fig. 26. a) Left contact angle and b) Right contact angle, as a function of time for an electric field experiment: $P = 600$ mbar, $T_{\text{sub}} = 5$ °K, $HF = 1.0$ W/cm², $UHV = 15$ kV, $t_{\text{wait}} = 10$ s.

close to the heater. The second goal is only achieved when the geometrical fitting is applied to trusted bubble contour regions that are away from the thermal boundary layer and do not suffer refractive distortion (as in the case of IMFT and AUTH/TUD/FORTH circle fittings).

Since the bubble shape is spherical for pool boiling case in microgravity conditions, the best method for bubble form approximation is a circle fit. For the shear flow case the bubble is deformed and we can approximate the bubble shape at contact points by two circles in the main flow direction. For the electric field case, the bubble is deformed and the bubble shape can be well approximated by an ellipse from which the contact angle can be determined.

The comparison of the bubble geometric features resulting from the different algorithms reveals that the efficiency of each approach depends on the nature of the measurement. To measure the characteristic dimensions (contact line diameter, bubble diameter, bubble height) of Multiscale Boiling bubbles that are larger than 1 mm, there is no need to apply complex image processing algorithms. These dimensions can be determined pretty accurately when applying conventional boundary fit codes. For Multiscale Boiling bubbles smaller than 1 mm, the measurement error is significant compared to the measured quantity and thus, measuring accuracy increases with the complexity of the method.

In this case, the error is either attributed to light reflections, or, in case of bubble diameter measurements, to the indirect nature of equivalent diameter calculations that derive from boundary fittings. From another perspective, thermal refraction triggers misdetection of contact points location and bubble curvature close to bubble foot resulting in over-estimated contact angle values. Hence, the accurate measurement of bubble contact angles requires the application of an algorithm that is able to treat both light reflections and refractive image distortion at the contact point regions.

5. Conclusions

In the present work, research teams from the University of Pisa (UNIPI), the Aix Marseille University (AMU) together with the Kutateladze Institute of Thermophysics (IT), the Institute of Fluid Mechanics of Toulouse (IMFT), and the Aristotle University of Thessaloniki (AUTH) together with the Technical University of Darmstadt (TUD) and the Foundation of Research and Technology (FORTH) in Crete, develop their own, specialized image processing algorithms, to process the image data obtained during ESA Multiscale Boiling Experiment that studies subcooled boiling in microgravity.

The optical setup of Multiscale Boiling Experiment suffers some

limitations, in that the background light reflects over the surface of the growing bubble, creating regions in which the boundary detection with traditional methods is troublesome, especially for large spherical bubbles in pool boiling. Furthermore, the optical distortion generated by the non-uniform temperature field in the surrounding fluid must be accounted for. To circumvent these drawbacks, the best way was sought to detect the bubble contour in order to measure the time evolution of the desired bubble geometry characteristics: diameter, volume, contact line diameter, and contact angle, for different operating conditions. Two fundamental approaches were analyzed: in the first the bubble contour is detected with traditional image processing methods (Canny or threshold), in the second a pre-determined geometrical shape is fitted around the contour.

The uncertainties of the evaluated bubble characteristics are quite small whatever is the method (boundary, circle, ellipse fit) and the code (UNIPI, AMU/IT, IMFT, and AUTH/TUD/FORTH) except for the contact angle measurement that depends on refractive optical distortion. For contact angle evaluation, the approximations of bubble form with standard geometries have to be used.

BW raw image data of benchmark Multiscale Boiling Experiment runs under study are published, for other research teams to test and evaluate their own codes further.

Declaration of Competing Interest

The authors declare the following financial interests/personal relationships which may be considered as potential competing interests.

Acknowledgments

The present work has been carried out in the framework of the

Appendix A. Calculation of bubble apex curvature with UNIPI method

The UNIPI algorithm offers the calculation of the radius of curvature of the bubble apex. This calculation is very sensitive to noise, as it depends on the second derivative of bubble contour. For the analytical calculation of bubble apex curvature, a parabola interpolates a series of 20 consecutive pixels (fine-tuned value) at the top part of the bubble contour. To improve the results, a weighted parabolic fit is applied. The parabola weights vary linearly along its arc, from 0 at the parabola center to 1 at parabola's extrema (see Fig. A1).

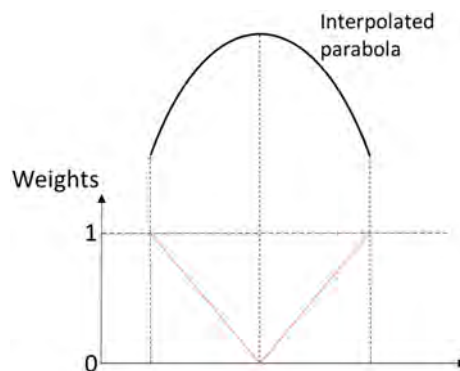


Fig. A1. Weights distribution along the parabola interpolating bubble apex.

Appendix B. Force balance analysis on bubble contour detection with IMFT method

IMFT research team applies a force balance in the vertical direction, to test the performance of different contour fittings for pool and shear flow boiling bubbles. Force calculations are presented at section S1 of the supplementary material.

In the case of boundary fit, it is found that the net force F_T, γ is unbalanced ($\neq 0$) both in the cases of pool boiling and shear flow (see Figs. B1a and B1b, black color line), which is not physically acceptable in microgravity conditions. This large deviation from the net force balance can be primarily attributed to the overestimation of the contact angles on the detected bubble boundary.

European Space Agency Research projects AO-2004-111: BOILING, AO-1999-110: EVAPORATION, AO-2004-096: CONDENSATION. We thank all the Multiscale Boiling Science Team Members of the different institutions for their contribution in making possible the implementation of the experiment on-board the International Space Station:

Technical University of Darmstadt, Institute for Technical Thermodynamics; Aix-Marseille University, IUSTI; University of Pisa; Institute of Thermal-Fluid Dynamics, ENEA; Institut de Mécanique des Fluides de Toulouse; Aristotle University of Thessaloniki; Transfers Interfaces and Processes, Université Libre de Bruxelles; University of Ljubljana; Kutateladze Institute of Thermo-physics, Novosibirsk.

The authors would also like to gratefully thank ESA, and in particular Daniele Mangini, Olivier Minster, Anne Pacros, Balazs Toth, and Marco Braibanti for their interest and support to the activities linked to Multiscale Boiling, and for the fruitful discussions. They would also like to thank AIRBUS (with particular gratitude to the project manager, Olaf Schoele-Schulz), as well as B.USOC for the kind cooperation (and especially Carla Jacobs and Denis Van Hoof) during all the pre-flight, in-flight and post-flight operations.

Co-authors from the Institute of Fluid Mechanis of Toulouse would like to thank the French Space Agency CNES for its support through the post-doc grant of Q. Raza, and funding, and organization of the parabolic flight campaigns.

Co-authors from the Kutateladze Institute of Thermophysics would like to acknowledge funding by the Russian Science Foundation, projects No. 21-79-10357 (development of the processing technique) and 19-19-00695 (analysis of the experimental results).

Co-authors from the Technical University of Darmstadt would like to thank the German Aerospace Center (DLR) for the financial support in the framework of the Vapor II project, grant no. 50WM1959.

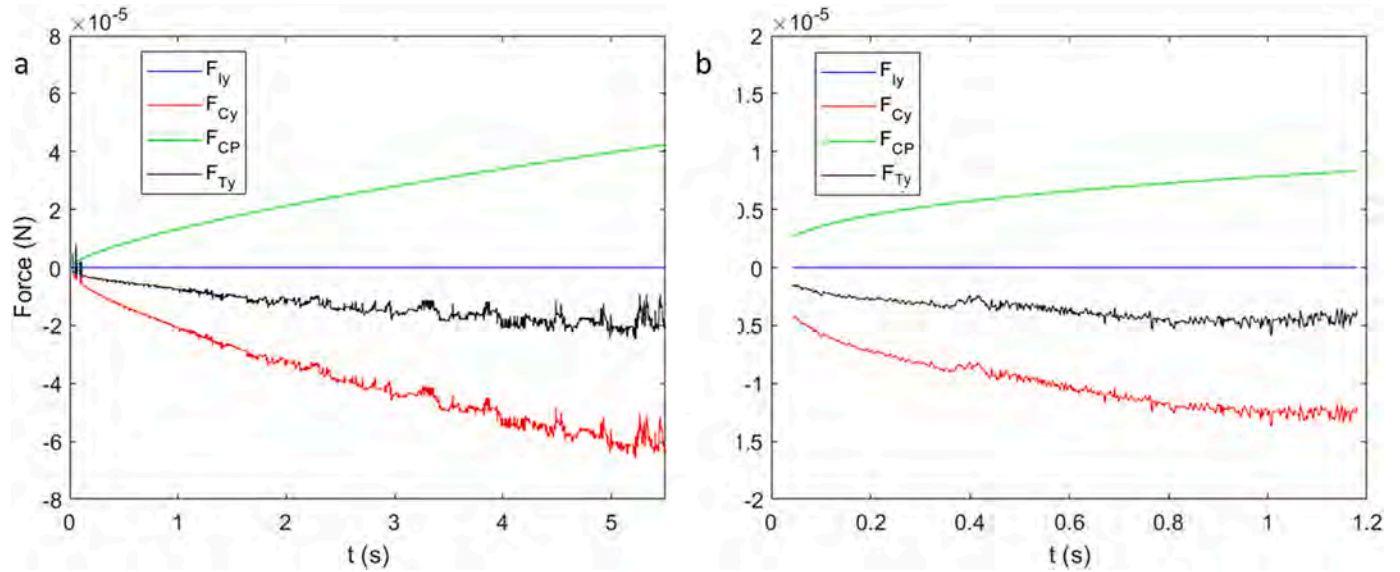


Fig. B1. Temporal evolution of various forces acting on the bubble during a) Pool boiling at $HF = 1 \text{ W/cm}^2$, $P = 750 \text{ mbar}$, $T_{\text{sub}} = 3 \text{ K}$ and b) Boiling in shear flow at $HF = 1 \text{ W/cm}^2$, $P = 1000 \text{ mbar}$, $T_{\text{sub}} = 3 \text{ K}$ and $Q = 500 \text{ ml/min}$.

Similarly, the circle fit and side circle fit approaches, show that the resulting net forces $F_{T, y}$ for the corresponding pool boiling and shear flow cases are insignificant (Fig. B2, black color line), and thus agree well with bubble growth in microgravity. Concluding, fitting bubbles contour with standard geometrical shapes to cope for refraction, seems to provide more realistic contact angle estimation.

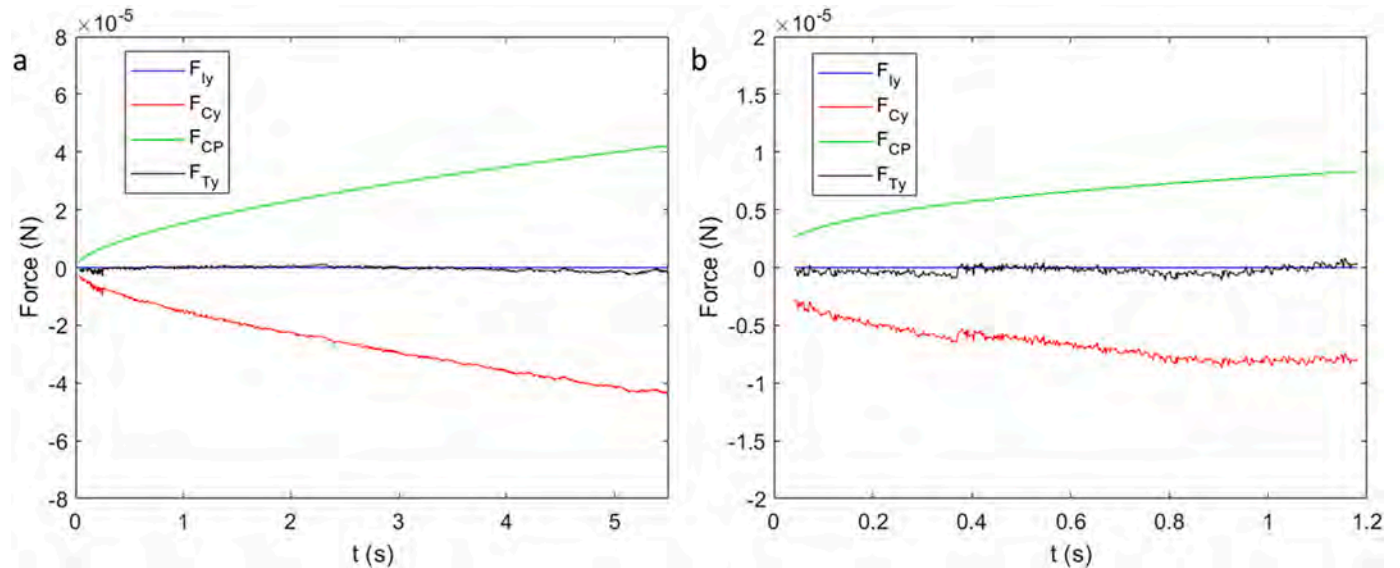


Fig. B2. Temporal evolution of various forces acting on the bubble based on the contact angle evaluation using a) circle fit approach for pool boiling at $HF = 1 \text{ W/cm}^2$, $P = 750 \text{ mbar}$, $T_{\text{sub}} = 3 \text{ K}$ and b) side circle approach for boiling in shear flow at $HF = 1 \text{ W/cm}^2$, $P = 1000 \text{ mbar}$, $T_{\text{sub}} = 3 \text{ K}$ and $Q = 500 \text{ ml/min}$.

Supplementary data to this article can be found online at <https://doi.org/10.1016/j.pdisas.2021.100193>.

References

- Mathew J, Krishnan S. *J Electron Packag* 2021;144(1):010801.
- Gao J, Proulx F, Rodriguez MJ. *Chemosphere* 2020;261:127531.
- Zhang F. *Int J Heat Technol* 2021;39(3):787–96.
- Ilic J, Tomasevic I, Djekic I. *Int J Gastron Food Sci* 2021;25:100401.
- Forster HK, Zuber N. *J Appl Phys* 1954;25(4):493–500.
- Engelberg-Forster K, Greif R. *J Heat Transf* 1959;81(1):43–52.
- Kutateladze SS. *Int J Heat Mass Transf* 1961;4:31–45.
- Han CY, Griffith P. *Int J Heat Mass Transf* 1965;8(6):887–904.
- Potash M, Wayner PCJ. *Int J Heat Mass Transf* 1972;15:1851–63.
- Stephan PC, Busse CA. *Int J Heat Mass Transf* 1992;35:383–91.
- Ajaev VS, Kabov OA. *Int J Heat Mass Transf* 2017;108:918–32.
- Schweizer N, Stephan P. *Multiph Sci Technol* 2009;21:329–50.
- Karchevsky AL, Marchuk IV, Kabov OA. *Appl Math Model* 2016;40:1029–37.
- Gibbons M, Di Marco P, Robinson AJ. *Int J Heat Mass Transf* 2018;121:641–52.
- Jo J, Kim J, Kim SJ. *Energy Convers Manag* 2019;181:331–41.
- Schweikert K, Sielaff A, Stephan P. *Interf Phenomena Heat Transf* 2019;7:269–81.
- Stephan K, Abdelsalam M. *Int J Heat Mass Transf* 1980;23(1):73–87.
- Stephan P. *B1 fundamentals of heat transfer*. Berlin Heidelberg, Berlin, Heidelberg: Springer; 2010.
- Iceria DM, Zummo G, Saraceno L, Ribatski G. *Int J Heat Mass Transf* 2020;153:119614.
- Wang X, Du Y, Tang Y, Liu L, Liu B, Zhang B, et al. *Exp Thermal Fluid Sci* 2022;134:110603.
- Lee J, Mudawar I, Hasan MM, Nagra HK, Mackey JR. *Int J Heat Mass Transf* 2022;183(Part C):122237.
- Siegel R. *Adv Heat Tran* 1967;4:143–228.
- Oka T, Abe Y, Tanaka K, Mori YH, Nagashima A. *Jpn Soc Mech Eng* 1992;35(2):280–6.
- Ohta H, Azuma H, Inoue K, Kawasaki K, Okada S, Yoda S, et al. In: *Heat Transfer in Nucleate Pool Boiling under Microgravity Condition2*; 1998. p. 401–6.

- [25] Colin C, Kannengieser O, Bergez W, Lebon M, Sebilleau J, Sagan M, et al. *Comp Rendus Mecanique* 2017;345:21–34.
- [26] Warriar GR, Dhir VK, Chao DF. *Int J Heat Mass Transf* 2015;83:781–98.
- [27] Raj R, Kim J, McQuillen J. *J Heat Transf* 2010;132(9):091502.
- [28] Sielaff A, Mangini D, Kabov O, Raza MdQ, Garivalis AI, Zupancic M, et al. *Appl Therm Eng* 2022;117932.
- [29] Di Marco P, Kurimoto R, Saccone G, Hayashi K. *A Tomiyama* 2013;49:160–8.
- [30] Jin Y, Miller DJ, Qiao S, Rau A, Kim S, Cheung FB, et al. *Nucl Eng Des* 2018;326: 202–19.
- [31] Serdyukov V, Malakhov I, Surtaev A. *J Vis* 2020;23(5):873–84.
- [32] Akbari R, Antonini C. *Adv Colloid Interf Sci* 2021;294:102470.
- [33] Narayan S, Srivastava A, Singh S. *Int J Heat Mass Transf* 2018;120:127–43.
- [34] Narayan S, Srivastava A, Singh S. *Int J Multiphase Flow* 2019;110:82–95.
- [35] Narayan S, Singh T, Singh S, Srivastava A. *Int J Heat Mass Transf* 2019;134: 85–100.
- [36] Franz B, Sielaff A, Stephan P. *Microgravity Sci Technol* 2021;33:27.
- [37] Cooper MG. *Int Heat Mass Transf* 1983;26(7):1088–90.
- [38] Canny J. *IEEE Trans Pattern Anal Mach Intell* 1986;8(6):679–98.
- [39] Di Marco P, Morganti N, Saccone G. *Journal of Physics: Conference Series* 2015; 655:012044.
- [40] Duhar G, Colin C. *Phys Fluids* 2006;18:077101.
- [41] Lebon M, Sebilleau J, Colin C. *Phys Rev Fluids* 2018;3:073602.
- [42] Lacassagne L, Zavidovique B. *J Real-Time Image Proc* 2011;117-135:2011.
- [43] Dillencourt MB, Samet H, Tamminen M. *J Assoc Comput Mach* 1992;39(2):253–80.